

The Response of the Sea Ice Edge to Atmospheric and Oceanic Jet Formation

HAROLD D. B. S. HEORTON AND DANIEL L. FELTHAM

Centre for Polar Observation and Modelling, Department of Meteorology, University of Reading, Reading, United Kingdom

JULIAN C. R. HUNT

Centre for Polar Observation and Modelling, University College London, London, United Kingdom

(Manuscript received 30 July 2013, in final form 8 May 2014)

ABSTRACT

The sea ice edge presents a region of many feedback processes between the atmosphere, ocean, and sea ice (Maslowski et al.). Here the authors focus on the impact of on-ice atmospheric and oceanic flows at the sea ice edge. Mesoscale jet formation due to the Coriolis effect is well understood over sharp changes in surface roughness such as coastlines (Hunt et al.). This sharp change in surface roughness is experienced by the atmosphere and ocean encountering a compacted sea ice edge. This paper presents a study of a dynamic sea ice edge responding to prescribed atmospheric and oceanic jet formation. An idealized analytical model of sea ice drift is developed and compared to a sea ice climate model [the Los Alamos Sea Ice Model (CICE)] run on an idealized domain. The response of the CICE model to jet formation is tested at various resolutions.

It is found that the formation of atmospheric jets at the sea ice edge increases the wind speed parallel to the sea ice edge and results in the formation of a sea ice drift jet in agreement with an observed sea ice drift jet (Johannessen et al.). The increase in ice drift speed is dependent upon the angle between the ice edge and wind and results in up to a 40% increase in ice transport along the sea ice edge. The possibility of oceanic jet formation and the resultant effect upon the sea ice edge is less conclusive. Observations and climate model data of the polar oceans have been analyzed to show areas of likely atmospheric jet formation, with the Fram Strait being of particular interest.

1. Background

Over sea ice, winds and ocean currents can compact the sea ice to produce a relatively narrow sea ice edge region. This occurs in the marginal ice zone (MIZ) lying between the open ocean and the continuous sea ice pack. The width of the MIZ is about 5–100 km and is characterized by ice floes that have been broken by wave energy from the open ocean (Lu et al. 2008). These floes are 5–500 m wide, 0.1–5 m thick, and are relatively free to drift compared to the larger and thicker floes of the central ice pack (1–30 km in diameter; Herman 2010), which are heavily compacted. The broken floes of the MIZ create a rougher surface for atmosphere and ocean flows compared to both the open ocean and sea ice pack

due to the form drag from the floe edges (Guest et al. 1995; Lüpkes et al. 2012). Understanding MIZ dynamics is needed to improve ice forecasting and climate modeling. There are many complex interactions within the MIZ aside from dynamics including sea ice melting and freezing and brine ejection (Pedersen and Coon 2004).

Atmospheric jets are known to form over coastlines with a band of faster wind centered over the shore (Houghton 1992). The atmospheric jets are colloquially known as “bends” to the wind (Simpson 2007). The formation of atmospheric jets can be described using models of wind flow over a sharp change in surface roughness (Hunt et al. 2004; Orr et al. 2005b). The theory presented by Hunt et al. (2004) considers wind jets formed over various surface roughness and elevation features. The model uses turbulent boundary layer theory (Belcher et al. 1993) considering processes that are of too small a scale to be resolved by current numerical climate models. Such an arrangement can be found at a sea ice edge far from land that has been

Corresponding author address: Harold D. B. S. Heorton, Centre for Polar Observation and Modelling, Department of Meteorology, University of Reading, P.O. Box 243, Reading, RG6 6BB, United Kingdom.
E-mail: h.heorton@reading.ac.uk

compacted by on-ice winds or ocean currents (Massom et al. 2008). The sea ice edge presents a similar change in surface roughness to that found at coast lines. The surface roughness lengths of both the sea ice edge (Guest and Davidson 1991) and a typical coast line (Jarmalavicius et al. 2012) are approximately 0.001–0.01 m. The surface roughness of the ocean surface is caused by wind-generated surface waves (Drennan et al. 2003). The maximum roughness length associated with the open-ocean surface is around 10^{-4} m, several orders less than over sea ice (Fairall et al. 2003). The theory of Hunt et al. (2004) defines a sharp change as a change over 1–10 km. This length scale is typical of a compacted sea ice edge (Massom et al. 2008). The theory of Hunt et al. (2004) requires a well-mixed atmospheric boundary layer (ABL) capped by a strong inversion. This atmospheric structure has been observed over the sea ice edge during on-ice surface winds in both the Arctic (Vihma et al. 2003; Vihma and Brummer 2002; Brummer et al. 1994) and Antarctic (Andreas et al. 2000).

For validation of the atmospheric jets there are studies of surface wind speed and direction. Sharp changes in wind stress have been predicted by Guest et al. (1995) as a cause of changes in the ABL. A sharp change in stress fits well with the second-order discontinuity in the wind speed perturbations (shown below in Fig. 4). Guest et al. (1995) also give observations of wind stress at the sea ice edge with the maximum just iceward of the sea ice edge during on-ice surface wind conditions in the Fram Strait. This is well correlated with a jet forming during winds at $90^\circ < \phi < 180^\circ$ to the ice edge. Orr et al. (2005b) attribute observed, sharp changes in cloud conditions over coastlines to the modeled sharp change in surface wind speed caused by jet formation. Such cloud conditions have been observed over the sea ice edge (Fairall and Markson 1987).

Atmospheric jet formation predicts changing wind speeds over an atmospheric Rossby radius. Guest et al. (1995) show changing surface wind speeds across the sea ice edges in the Antarctic and Arctic Oceans. Wind speeds are shown to vary over the order of 100 km from the sea ice edge during on-ice wind conditions. These events happened for surface wind speeds of $< 15 \text{ m s}^{-1}$ and so fit well with the atmospheric jets presented in this paper [low Froude number conditions require $U_A < 10.9 \text{ m s}^{-1}$ (see Table 1 for the definition of this and other variables that follow), but the perturbed wind speed can be greater than this]. The observations of Andreas et al. (1984) have a similar form.

The sea ice edge can also be a location of low-level jet formation (Vihma and Brummer 2002; Andreas et al. 2000). Low-level jets develop vertically with a peak wind speed at about 100 m above the ocean surface (as shown

TABLE 1. Key mathematical notation.

Notation	Description
x, y, z	Positional vector components
X, Y, Z	Scaled positional vector components
f_c	Coriolis parameter
ρ	Density
ϕ	Angle between flow and sea ice edge
U_A, U_O, U_I	Typical atmosphere, ocean, ice speeds
For section 2 and appendix specifically	
h_A, h_M	ABL and OML thickness
h, \hat{h}	Original, scaled layer thickness perturbation
U, V, W	Mean flow profile without jet
u', v', w'	Dimensional flow perturbations
\bar{u}, \bar{v}	Layer-averaged perturbations
\hat{u}, \hat{v}	Scaled perturbations
$P + p$	Flow pressure + pressure perturbation
(A, O)	A atmosphere, O ocean
$\tilde{U}_{(A,O)}, \tilde{V}_{(A,O)}$	Flow aligned dimensional velocity with jet
$\mathcal{L}_{R(A,O)}$	Rosby radii
$\mathcal{F}_{(A,O)}$	Froude numbers
$\Delta \rho_{(A,O)}$	Flow density step change
\bar{F}, \bar{G}	Layer-averaged body forces
\hat{F}, \hat{G}	Scaled body forces
$\Delta C_{(F,G)}$	Drag parameterization function
$\Delta \hat{C}_{(F,G)}$	Scaled drag parameterization
For section 3 specifically	
$\mathbf{u} = (u, v)$	Ice drift velocity vector
$\mathbf{u} = U_I(\hat{u}, \hat{v})$	Scaled ice drift velocity vector
$\hat{\tau}^a = \mathcal{T}_a \hat{\tau}^a$	Original, scaled applied atmospheric stress
$\hat{\tau}^o = \mathcal{T}_o \hat{\tau}^o$	Original, scaled applied oceanic stress
$\mathbf{T}_{(1,2)}[X, \hat{u}, \hat{v}]$	Combined applied stress component
A	Ice concentration
σ_{ij}	Internal ice stress component
$g(A)$	Ice strength or pressure function

in Fig. 1) and can be attributed to changing baroclinicity due to the jet's on-ice direction and the temperature difference between the open ocean and sea ice pack (Vihma and Brummer 2002) or through the decoupling of the atmosphere through stable stratification (Andreas et al. 2000). In both these cases, the low-level jet formation is linked to changing surface temperature and baroclinicity (the alignment of density and pressure gradients) and not changing surface roughness. Hunt et al. (2004) shows through the scaling analysis of drag and thermal body forces that perturbations driven by changes in surface roughness are of a significantly greater magnitude than those driven by thermal effects. Additionally, the occurrence of low-level jets does not significantly alter surface wind speed (Vihma and Brummer 2002) implying that for this study of atmosphere and sea ice interaction, baroclinicity can be neglected. However, thermal processes in the atmosphere above the sea ice should not be ignored. Chechin et al. (2013) show that during the winter, off-ice atmospheric

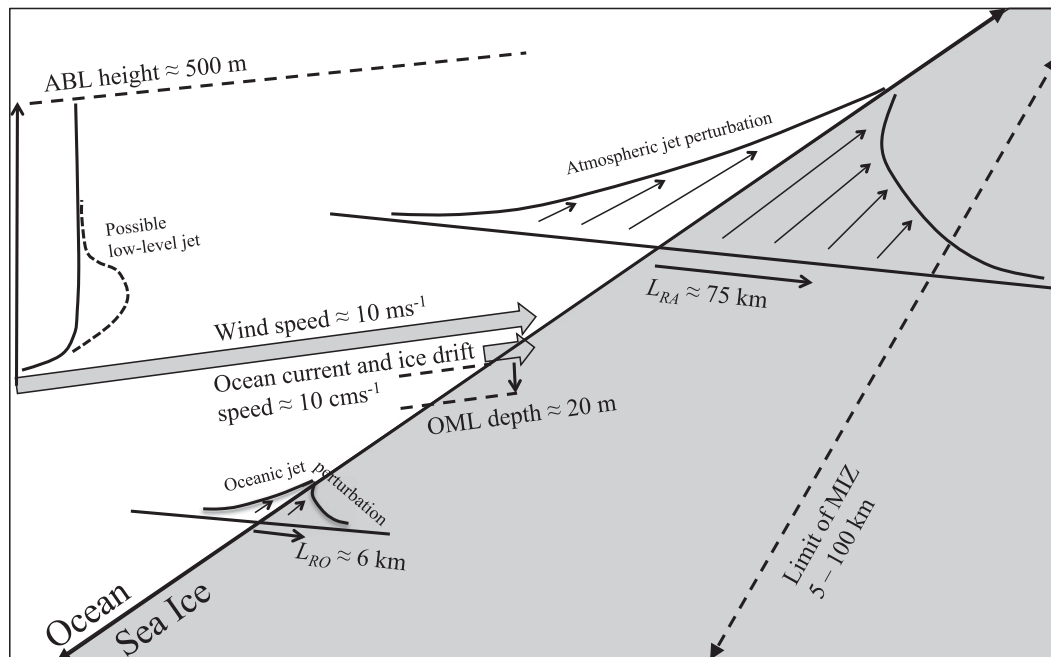


FIG. 1. The sea ice edge and MIZ from above, with the converging lines demonstrating perspective. This figure illustrates the difference in magnitude of the atmosphere, ocean, and ice speeds and the difference in size of the ABL and OML and the width of the ocean and atmosphere jets. The shape of low-level atmospheric jets is also shown, although not investigated in this paper.

flows can be strongly modified by thermal effects resulting in jet formation. Hunt et al. also comment that during certain situations thermal effects can dominate and block even a moderately strong approach flow that could be true for the strong thermal gradient between the open ocean and sea ice during winter months (Tisler et al. 2008). The theory presented in this paper is most applicable for the sea ice edge summer months when there is moderate baroclinicity, though further investigation is needed.

Ice jet formation at the sea ice edge has been observed. Johannessen et al. (1983) presents a study of sea ice drift using observations from buoys tethered to sea ice floes. These observations are from the sea ice edge and MIZ north of Svalbard in the Arctic Ocean. The sea ice drift is observed to be parallel to the sea ice edge and aligned with strong winds (see Fig. 2). The ice drift within 10 km from the open ocean is shown to be fastest with the drift speed decaying into the sea ice pack, reducing by half at 250 km from the sea ice edge. There have been attempts to show that the formation of the observed ice jets is due to interactions between individual ice floes. Lepparanta and Hibler (1985) applied the viscous plastic rheology of sea ice deformation of Hibler (1979) to an idealized ice edge and MIZ. Numerical and analytical simulations of ice drift during

uniform on-ice and along-ice winds were derived but did not result in an ice jet. By contrast, Feltham (2005) used granular flow theory to describe kinetic and slowly deforming granular flows over the MIZ, showing that an ice jet can form in a boundary layer at the extreme ice edge. This jet formation is on a small scale (over approximately 1 km) compared to the extent of the MIZ (typically 100 km) and not consistent with the wider jet observed by Johannessen et al. (1983).

In this paper we investigate whether the occurrence of sea ice drift jets can be attributed to atmospheric and oceanic jet formation during on-ice surface winds and ocean currents at the sea ice edge. To investigate jet formation at the sea ice edge, we first consider the atmospheric jet theory of Hunt et al. (2004) in section 2 with a summary of the essential theory given in the appendix. We present the novel adaptation of the model of atmospheric jet formation for the consideration of oceanic jet formation in section 2a. The scale and strength of the jets is calculated using parameter values and ambient characteristics taken from existing literature in section 2b. These calculations are used to prescribe the atmospheric and oceanic stresses in both analytical and numerical sea ice models. The analytical sea ice model has been derived for this study and is described in detail in section 3. The numerical model is the Los Alamos Sea

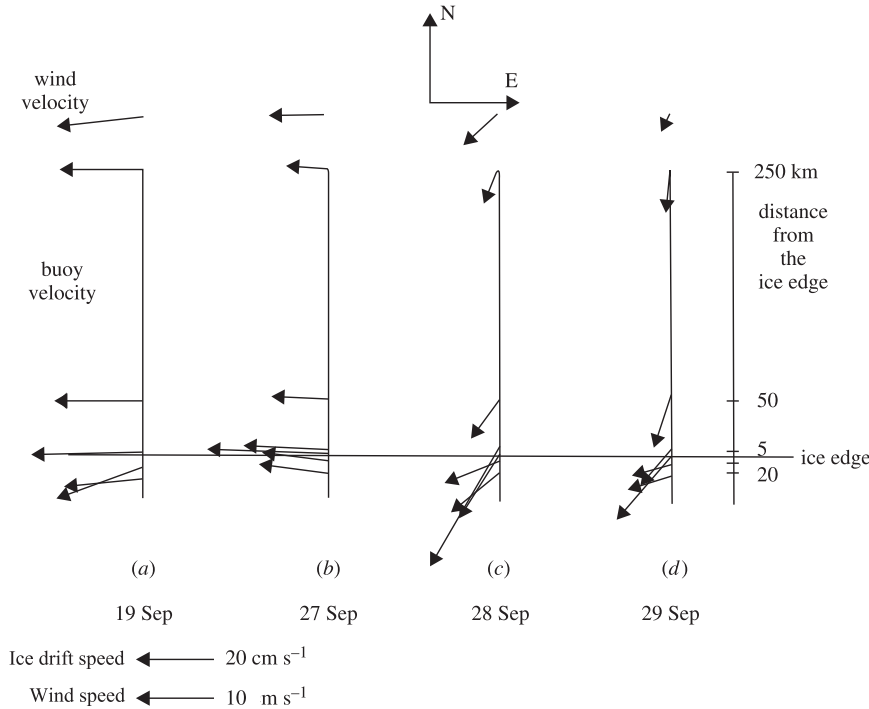


FIG. 2. Daily average ice drift and surface current from Argos drifting buoys and ship-measured wind on (a) 19 Sep, (b) 27 Sep, (c) 28 Sep, and (d) 29 Sep 1979 (from Johannessen et al. 1983). The spatial variation of the sea ice drift velocity in (a) and (b) is well correlated with the sea ice drift jet formation modeled in this paper.

Ice Climate Model (CICE) described in section 4. Simulations of ice drift jets from both models are presented in section 5. In section 6, we discuss the situations in which ice drift jets will typically form and the resulting impact upon the transport of sea ice along the sea ice edge. In section 7, we summarize our main conclusions.

2. Theory of jet formation

In this paper the jet formation theory of Hunt et al. (2004) is applied to a sea ice edge at an arbitrary angle to the wind direction (illustrated later in Fig. 4). We also present the application of the same theory to the ocean underneath the sea ice edge as described in section 2a. Key values for the length, velocity, and surface roughness for the atmospheric and oceanic jets are derived in section 2b. The background theory of Hunt et al. (2004) is presented in the appendix with original work within this section.

a. Theory of ocean jet formation

Turbulent stresses are assumed to exist within the ocean mixed layer (OML), and we derive model equations for ocean jet formation. The OML is modeled using the same shallow layer approximations described in

the appendix for the ABL with a further description in Hunt et al. (2004).

For the ocean model, an OML of density ρ_M and thickness h_M sits above the ocean of higher-density ρ_O as demonstrated in Fig. 3. The density step change between the two is $\Delta\rho_O = (\rho_O - \rho_M)/\rho_O$. A uniform current of strength U_O encounters the sea ice bottom (Ib) with roughness length z_{Ib} . The reduced gravitational acceleration of the flow is $\Delta g_O = g\Delta\rho_O$. This simple formulation of the mixed layer under the sea ice edge is similar to that used by Roed and O'Brien (1983).

As for the atmospheric jets in the appendix, the mean ocean current velocity profile [$U(z), V(z), W(z) = 0$] and perturbations to the flow (u', v', w') are calculated. The pressure profile and its perturbation are given as $P(z)$ and p . With this bulk model the mean profiles are uniform horizontally and the perturbations are uniform vertically. Upflow conditions at $x \rightarrow -\infty$ are assumed to be steady and uniform in the horizontal plane. The change in surface roughness perturbs the surface shear layer of thickness h_s . For the OML, there are perturbations at the ocean surface h_t and bottom of the mixed layer h_b (see Fig. 3). The changing turbulent stresses in the shallow layer are represented by the body forces $F(x, y, t)$ and $G(x, y, t)$ in the x and y directions, respectively.

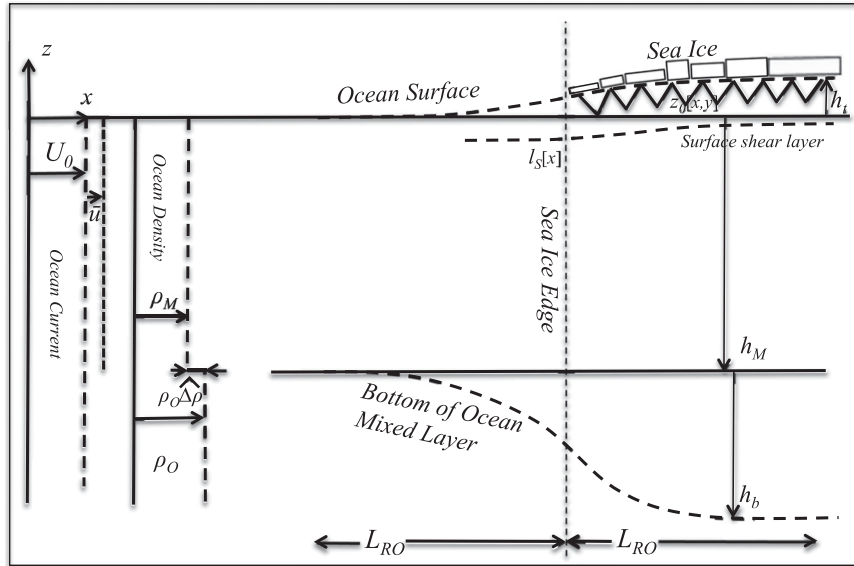


FIG. 3. Vertical profile of velocity $[U(x), \mathbf{u}]$ and density ρ_0 of the OML model described in section 2a. The presence of the sea ice edge perturbs the thickness of the OML by amount $h = h_t + h_b$, resulting in perturbation to ocean velocity of magnitude \bar{u} . The x axis is aligned with the far-field ocean current.

Velocity perturbations to the shallow layer are modeled by applying the momentum balance for velocity perturbations to the OML. Expressions for pressure ($P + p$), layer thickness perturbation $h = h_t + h_b$, and body forces (F, G) are obtained. The perturbation velocity w' at the top and bottom of the OML is equated to the change in layer thickness Dh with $Dh_t = w'|_{z=h_t}$ and $Dh_b = -w'|_{z=-(h_M+h_b)}$. The overall change in layer thickness is the sum of these $Dh = Dh_t + Dh_b$, which can be approximated by the velocity perturbation by integrating the continuity equation over the mixed layer giving

$$\begin{aligned} Dh &= w|_{z=h_t} - w|_{z=-(h_M+h_b)} \\ &= \int_{-(h_M+h_b)}^{h_t} w_z dz \approx -(\bar{u}_x + \bar{v}_y)h_M, \end{aligned} \quad (1)$$

where (\bar{u}, \bar{v}) are the perturbation velocities (u', v') averaged across the OML.

Pressure perturbations for the OML are as follows (illustrated in Fig. 3). For the OML at position (x, z) (with invariance in the y direction) the total pressure $(P + p)(x, z)$ is

$$(P + p) = (P + p)|_{z=h_t} + g(1 - \widehat{\Delta\rho_O})(h_t - z),$$

where

$$(P + p)|_{x \rightarrow -\infty} = (P + p)|_{z=0}^{x \rightarrow -\infty} + g(1 - \widehat{\Delta\rho_O})z,$$

in the open ocean away from the influence of any ocean jet. The sea surface pressure P_s is taken to be independent of position with

$$(P + p)|_{z=h_t} = (P + p)|_{z=0}^{x \rightarrow -\infty} = P_s.$$

Furthermore, pressure at equal depths below the OML is assumed to be equal throughout the model with

$$(P + p)|_{z=-(h_M+h_b)}^{x \rightarrow -\infty} = (P + p)|_{z=-(h_M+h_b)},$$

$$\begin{aligned} P_s + g(1 - \widehat{\Delta\rho_O})h_M + gh_b \\ = P_s + g(1 - \widehat{\Delta\rho_O})(h_t + h_M + h_b), \end{aligned}$$

$$\text{which gives } \widehat{\Delta\rho_O}h_b = (1 - \widehat{\Delta\rho_O})h_t. \quad (2)$$

Thus, the thickness of the OML is linked to the raised sea surface with $h = h_t/\widehat{\Delta\rho_O}$. As the density inversion is of order 10^{-3} and the mixed layer is of order 10 m thick, the change in sea surface level h_t will be of order 10^{-2} m. This change happens over a Rossby radius (10^4 m) and will be almost undetectable. See section 2b for derivation of numerical values.

The pressure perturbation can now be given by

$$(P + p) - (P + p)|_{x \rightarrow -\infty} = p(z) = g(1 - \widehat{\Delta\rho_O})h_t \approx \Delta g_O h$$

to leading order. The horizontal pressure gradients are

$$\begin{aligned} p_x &= \Delta g_O h_x \quad \text{and} \\ p_y &= \Delta g_O h_y, \end{aligned} \quad (3)$$

which are analogous to the pressure gradients in the ABL. Combining the pressure perturbations and body forces and averaging over the mixed layer $[-(h_M + h_b) < z < h_I]$ we get Eq. (A2) with the substitution $\Delta g_A \rightarrow \Delta g_O$ with the full derivative $D = \partial/\partial t + U_O \partial/\partial x$. The scaling values for the OML flow are the oceanic Froude number $\mathcal{F}_O = U_O/\sqrt{\Delta g_O h_M}$ and the oceanic Rossby radius $\mathcal{L}_{RO} = \sqrt{\Delta g_O h_M}/f_c$, where f_c is the Coriolis parameter.

For the OML, the converse to the drag-dependent body forces $F[x, y, t]$, $G[x, y, t]$ is the drag experienced by sea ice from the ocean that is given as

$$\tilde{\tau}^O = \rho_o C_O |\mathbf{U}^O - \mathbf{u}| [(\mathbf{U}^O - \mathbf{u}) \cos \theta + \mathbf{k} \times (\mathbf{U}^O - \mathbf{u}) \sin \theta] \quad (4)$$

(e.g., Feltham 2005), where \mathbf{U}^O is the ocean velocity, \mathbf{u} is the ice velocity, θ is a turning angle, ρ_o is the density of seawater, and C_O is a constant associated with the drag between the ocean and ice. The turning angle is used to parameterize the Ekman turning of the water column underneath the ice. As the turning angle ϕ is typically small and neglected in models, here we simplify the consideration of the OML by setting θ to zero. For the ABL, the stress applied to the ice from the atmosphere is calculated from the wind speed (as used in the sea ice models in sections 3 and 4) with

$$\tilde{\tau}^A = \rho_a C_A |\mathbf{U}^A| \mathbf{U}^A, \quad (5)$$

where ρ_a is the air density, \mathbf{U}^A is the wind speed, and C_A is a drag coefficient (Csanady 2001). The terms C_A and \mathbf{U}^A refer to winds at a certain height. For this study a height of 10 m is used. Typical surface wind speeds over sea ice (of order 10 m s^{-1} ; Vihma and Brummer 2002) are two orders of magnitude greater than typical sea ice drift speeds (of order 0.1 m s^{-1} ; King et al. 2010), allowing Eq. (5) to be dependent upon the wind speed only. Because typical ocean current speeds are of the same order of magnitude as sea ice drift speeds (Fer and Sundfjord 2007), Eq. (4) has to consider the difference between the ocean current and sea ice drift velocities to give the correct magnitude and direction of applied stress. For example, when the ocean current and sea ice drift have equal velocity there is no applied stress from ocean to sea ice and vice versa. Therefore, Eqs. (A7) cannot be used for the body forces in the OML shallow layer model. The flow velocity term in these equations needs to be replaced with the relative difference in velocity between the ocean and ice. This is done by introducing

$$u_{\text{diff}}^2 = |\hat{\mathbf{U}}_O - \hat{\mathbf{U}}_I|^2, \quad (6)$$

where $\hat{\mathbf{U}}_{O,I}$ are the typical nondimensional velocities of the ocean and sea ice at the sea ice edge. The selection of values for $\hat{\mathbf{U}}_{O,I}$ requires the coupling of the ocean jet calculation to a sea ice model as described in section 3b. The OML body forces are

$$\begin{aligned} \bar{F} &= -\frac{\Delta C_F U_O^2 u_{\text{diff}}^2}{h_M} \quad \text{and} \\ \bar{G} &= -\frac{\Delta C_G U_O^2 u_{\text{diff}}^2}{h_M}, \end{aligned} \quad (7)$$

selecting appropriate forms for the functions ΔC_F and ΔC_G that parameterize the drag strength and direction due to surface characteristics as described in Eq. (A8) and onward. The ocean jet model is created analogously to the atmospheric jet model in Eqs. (A2)–(A14) by replacing Eq. (A7) with Eq. (7) and scaling over the OML. This adaptation of the forcing functions only alters the magnitude of the drag and whether the drag is acting with or against the current. The velocity-dependent body force Δu , which is neglected from Eq. (A8) onward, could play a greater role in this formulation of the OML than it does for the ABL. This could be considered in further study.

b. Application of the jet formation theory to the sea ice edge

To calculate the size and strength of the jets over the sea ice edge, numerical values are needed. For the atmosphere the Froude number and Rossby radius are dependent upon the thickness of the ABL and the strength of the inversion at the top of it. There are observations of atmospheric processes over sea ice from which these values can be taken.

The ABL height over the MIZ is widely documented. The inversion height is low, varying from 200 (Vihma et al. 2003; Brummer et al. 1994) to 500 m (Guest et al. 1995; Andreas et al. 1984). Considering the modification to the inversion height due to jet formation (Fig. 4) and observations of the ABL height over the ocean near the sea ice edge (500 m; Fairall and Markson 1987), a value of $h_A = 400 \text{ m}$ is used in our calculations.

The inversion strength at the top of the ABL is less widely documented. This is due to the difficulty in observing such a change. The most common observations are in the form of a step change in potential temperature. This change ranges from 5° (Guest et al. 1995; Kantha and Mellor 1989) to 10°C (Tjernström 2005; Andreas et al. 1984). The change in potential temperature can be equated to the inversion layer strength defined by $\widehat{\Delta \rho}_A = \Delta T/T_A$ (Garratt 1992), where ΔT is

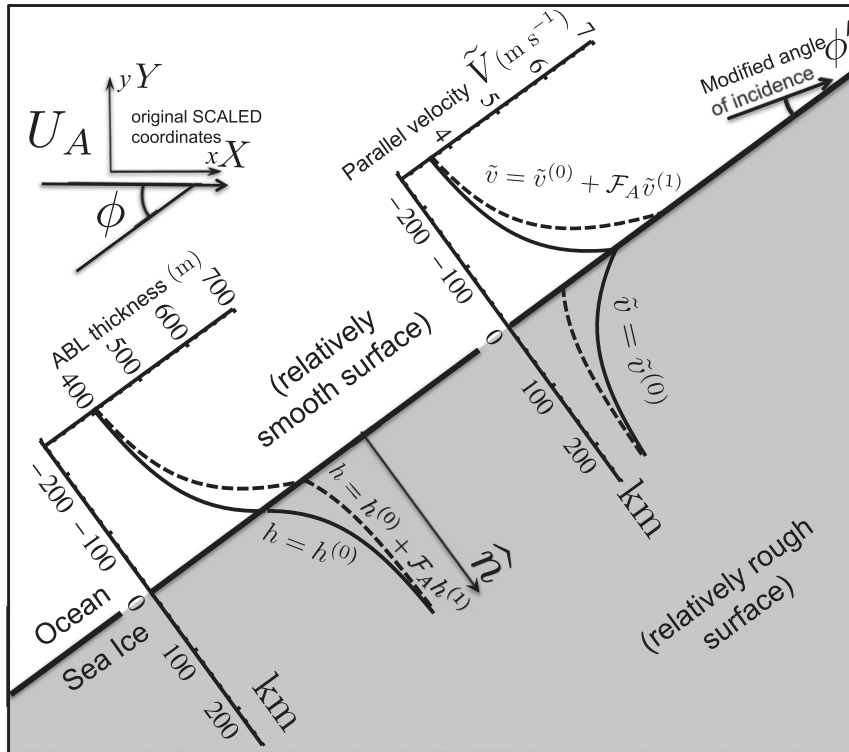


FIG. 4. Atmospheric flow of speed U_A over a sharp change in surface roughness at angle ϕ to the flow viewed from above. The ABL thickness h and flow velocity parallel to the sea ice edge [\tilde{V} in Eq. (8b)] for wind speed $U_A = 5 \text{ m s}^{-1}$ at angle $\phi = 45^\circ$ with a Froude number of $\mathcal{F}_A \approx 0.5$ in the Northern Hemisphere is plotted. The plotted perturbations to the flow are over an order of Rossby radius L_{RA} either side of the change in surface roughness, resulting in a modified angle of incidence ϕ' for the perturbed flow. The plotted profiles are for the first order ($\tilde{v} = \tilde{v}^{(0)}$, solid lines) and second order ($\tilde{v} = \tilde{v}^{(0)} + \mathcal{F}_A \tilde{v}^{(1)}$, dashed lines).

the change in potential temperature and T_A is the atmospheric potential temperature in degrees Kelvin. The range of observed values give $0.18 < \Delta\rho_A < 0.35$. A typical value of 0.3 is used here. The selected values of $\Delta\rho_A$ and h_A result in the wave speed along the top of the ABL as $\sqrt{\Delta g_A h_A} \approx 10.9 \text{ m s}^{-1}$. The atmospheric Rossby radius is calculated as $\mathcal{L}_{RA} = \sqrt{\Delta g_A h_A} / f_c \approx 75 \text{ km}$. The condition for low Froude number flows ($\mathcal{F}_A < 1$) is that $U_A < 10.9 \text{ m s}^{-1}$.

The surface roughness length of sea ice is often given a value of $z_A = 0.001 \text{ m}$ in atmospheric models (Vihma et al. 2003), though this value is a product of sensitivity studies (Csanady 2001). The value associated with the sea ice pack is too low for the broken MIZ. Tisler et al. (2008) investigates this parameter and uses a value of $z_A = 0.01 \text{ m}$ for rougher ice. The thickness of the shear layer h_s is an observed and modeled value for the MIZ. It is consistent over several studies at approximately 20 m (Tisler et al. 2008; Kantha and Mellor 1989). These values give $\Delta C_F \approx 3 \times 10^{-3}$ [Eq. (A8)]. This value is comparable to drag coefficients that have

been measured over the MIZ. Anderson (1987) measured $C_{10} \approx 3.5 \times 10^{-3}$ (10-m drag coefficient) using direct eddy flux measurements. This is also in agreement with Bennett and Hunkins (1986) who analyzed the expedition of Andreas et al. (1984), the review of Guest et al. (1995), and the drag modeling of Birnbaum and Lupkes (2002). The studies of Birnbaum and Lupkes (2002) and Lüpkes and Birnbaum (2005) analyze various drag laws including form drag (the drag from floes edges) against ice concentration with a maximum 10-m drag given at 80% ice concentration that fits with the more detailed formulation of Lüpkes et al. (2012) and our chosen value of $\Delta C_F \approx 3 \times 10^{-3}$ for the MIZ.

Using the values derived above, the size and strength of the atmospheric jets can be calculated from Eqs. (A11)–(A14). First, we seek a solution for the perturbation to the ABL thickness. For the Northern Hemisphere, solutions give an increasing on-ice ABL thickness over the scale of \mathcal{L}_{RA} for $0 < \phi < \pi/2$, as shown in Fig. 4, and decreasing mixed layer thickness for $\pi/2 < \phi < \pi$. This is reversed for the Southern

Hemisphere. The leading-order term $\hat{h}^{(0)}$ gives a monotonic solution across the roughness change. The first-order correction $\hat{h}^{(1)}$ adds a localized peak centered over the roughness change. The shape of the change in ABL thickness is that of the functions $J^{(1,2)}$ as described in Eq. (A12b). The ABL perturbation $\hat{h} = \hat{h}^{(0)} + \mathcal{F}_A \hat{h}^{(1)}$ can now be used in Eq. (A13) to give velocity perturbations aligned to the unperturbed flow given in Eq. (A14). Adding the original flow and rotating the components gives the dimensional values for the wind velocity components perpendicular \tilde{U}_A and parallel \tilde{V}_A to the ice edge (see Fig. 4) as

$$\tilde{U}_A = U_A \sin\phi \quad \text{and} \quad (8a)$$

$$\tilde{V}_A = U_A \cos\phi + U_A \frac{\Delta C_F \mathcal{L}_{RA}}{h_A \tan\phi} \left[J^{(0)'}(\hat{n}) + \mathcal{F}_A \frac{J^{(1)'}(\hat{n})}{\cos\phi} \right], \quad (8b)$$

with the functions $J^{(0,1)'}$ as defined in the appendix. Note that the velocity perturbation perpendicular to the sea ice edge $\tilde{u} = -\hat{u} \sin\phi + \hat{v} \cos\phi$ is always zero as $\hat{u} \cos\phi \equiv \hat{v} \sin\phi = \widehat{\Delta C_F / \mathcal{F}_A} \cos^2\phi(\dots)$, leaving the component of the total wind velocity perpendicular to the sea ice edge unchanged by the jet formation.

The jet formed is approximately 200 km wide, with smaller perturbations covering 600 km. The jet is more intense for the ocean side of the roughness change seen in the dashed second-order correction plotted in Fig. 4. This is reversed for $90^\circ < \phi < 180^\circ$ due to the antisymmetrical first-order correction $[J^{(1)' }(\hat{n})]$ in Eq. (8b), which also depends upon the sign of the Coriolis acceleration resulting in a reversed angular dependence for the Southern Hemisphere. The wind speed increases about the sea ice edge, causing a change in wind direction ϕ' . The change in wind direction turns the wind more parallel to the ice edge for all values of ϕ and in both hemispheres. For faster wind speeds, the Froude number increases, creating a larger antisymmetry in the jet and faster peak wind speeds (as seen in the results discussed in section 5a).

The parallel component of the wind velocity increases rapidly as the upstream flow becomes parallel to the ice edge ($\phi \rightarrow 0$ or $\phi \rightarrow 180$) that can be seen in the atmospheric velocity enhancement shown below in Fig. 8a. This increase is due to the inverse $\tan\phi$ relationship in Eq. (8b) and is not realistic as a flow parallel to the ice edge requires a different mathematical analysis, as described by Hunt et al. (2004). Parallel flows are continually accelerated as they flow along the edge. The maximum perturbation to the flow depends on the length of the ice edge. For parallel flows, Hunt et al.

(2004) give the relationship between the maximum dimensional parallel perturbation and edge length as

$$\bar{v} = U_A \frac{\Delta C_F l}{2h_M}, \quad (9)$$

where l is the dimensional length of the ice edge. A length of $l = 250$ km is used in these calculations to represent the persistence of winds that form parallel to the ice edge. This is in accordance with the winds and ice edge state observed during on-ice winds (Massom et al. 2006, 2008; King et al. 2010). Another limiting factor is the straightness of the ice edge. The edge of the ice pack is unlikely to form a straight edge and is more likely to meander and appear rough. A purely parallel flow is unlikely to persist for longer than a Rossby radius. An angle limit of 5° will be used in these calculations, limiting the size of the perturbation for angles of $0^\circ \leq \phi \leq 5^\circ$ and $175^\circ \leq \phi \leq 180^\circ$.

The characteristic scales associated with the OML ($\mathcal{L}_{RO}, \mathcal{F}_O$) are calculated from the density inversion and mixed layer thickness. These two values can be taken from observations of ocean salinity. We use a linearized equation of state for seawater:

$$\rho = \rho_0(1 - \alpha T + \beta S) \quad (10)$$

(e.g., Thorpe 2005), where ρ_0 is a reference ocean density, T is the temperature, and S is the salinity. The terms α and β are constants based on the expansion of water and are specified at reference values for S and T and vary with depth. For the mixed layer at the sea ice edge, we use Eq. (10) to calculate $\Delta\rho_O$ from changes in salinity ΔS and temperature ΔT , giving $\Delta\rho_O = -\alpha\Delta T + \beta\Delta S$. The parameters α and β are taken as $52 \times 10^{-6} \text{ deg K}^{-1}$ and 0.82 psu^{-1} , respectively, for seawater near its freezing temperature of -1.8°C . For the OML in polar regions, the change in salinity contributes most to the change in ocean density, although the characteristics of the OML vary with location and season, which could be considered in a larger study.

Measurements of mixed layer depth vary by some degree. For the sea ice pack over 100 km away from the open ocean, the mixed layer is typically 20–30 m deep and rarely exceeds 50 m (Toole et al. 2010; McPhee et al. 2005). By contrast, in the MIZ the mixed layer depth can vary from 25 m (Fer and Sundfjord 2007; Williams et al. 2008; Quadfasel et al. 1987) to as high as 150 m (Markus 1999; Padman and Dillon 1991). This variability in the mixed layer depth makes the selection of a value for h_M challenging. There is often a seasonal variation in the depth (Markus 1999), which could be included in coupled models with a time series over several years.

There is a good correlation between the depth of the mixed layer and the change in salinity. For a shallow

mixed layer, the salinity change was between 1.5 and 3 psu (Quadfasel et al. 1987; Toole et al. 2010; McPhee et al. 2005), whereas for a deeper mixed layer, it was lower at 1 psu (Padman and Dillon 1991). Average values of $h_M = 40$ m and $S = 2.5$ psu are taken. This gives a density change of $\rho_O \Delta \rho_O \approx 2 \text{ kg m}^{-2}$ that correlates well with values given by McPhee et al. (1987) and Toole et al. (2010). These values give $\sqrt{\Delta g h_M} \approx 0.9 \text{ m s}^{-1}$, which results in a Rossby radius of ≈ 6 km. The value of $\sqrt{\Delta g h_M}$ is high enough for low Froude number conditions for $U_0 < 0.9 \text{ m s}^{-1}$. This is true for all but the most extreme ocean currents.

There has been little study into the surface roughness of the underside of the MIZ. Shaw et al. (2008) conducted a study of roughness length measurements under the central Arctic pack ice: the typical roughness lengths were of $0.005 \text{ m} < z_{\text{lb}} < 0.03 \text{ mm}$. A value of $z_{\text{lb}} = 0.02 \text{ m}$ and a shear layer depth of $l_S = 4.5 \text{ m}$ give a value of $\Delta C_F \approx 0.0055$. This is equal to the value of C_O [see Eq. (4)] used by Feltham (2005). Shaw et al. (2008) also recorded roughness lengths of up to $z_{\text{lb}} = 0.15 \text{ m}$ for rougher sea ice due to the presence of pressure ridges. As the broken floes of the MIZ suggest a rougher surface than that of the sea ice pack, a value of $z_{\text{lb}} = 0.1 \text{ m}$ shall be used, giving $\Delta C_F \approx 0.011$.

The dimensional perturbations can now be calculated from Eq. (A14), giving the dimensional ocean current velocity components perpendicular \tilde{U}_O , and parallel \tilde{V}_O , to the sea ice edge as

$$\tilde{U}_O = U_O \sin \phi \quad \text{and} \quad (11a)$$

$$\tilde{V}_O = U_O \cos \phi$$

$$+ U_O \frac{\Delta C_F \mathcal{L}_{RO} u_{\text{diff}}^2}{h_M \tan \phi} \left[J^{(0)'}(\hat{n}) + \mathcal{F}_O \frac{J^{(1)'}(\hat{n})}{\cos \phi} \right]. \quad (11b)$$

They are of a similar form to the atmospheric jet solution in Eq. (8) with one major difference in the addition of the u_{diff}^2 term. The ocean jet is approximately 20 km wide. Knowledge of the sign and size of u_{diff}^2 is essential to modeling the ocean jets. If the ice is moving at the same velocity as the ocean, the ocean will experience no relative velocity to the change in surface roughness and no jet will form. The jet formation is best modeled by coupling the ocean jet formation to a dynamic sea ice model.

3. Analytical sea ice model

To model the response of sea ice drift to the atmospheric and oceanic jet formation presented in section 2a,

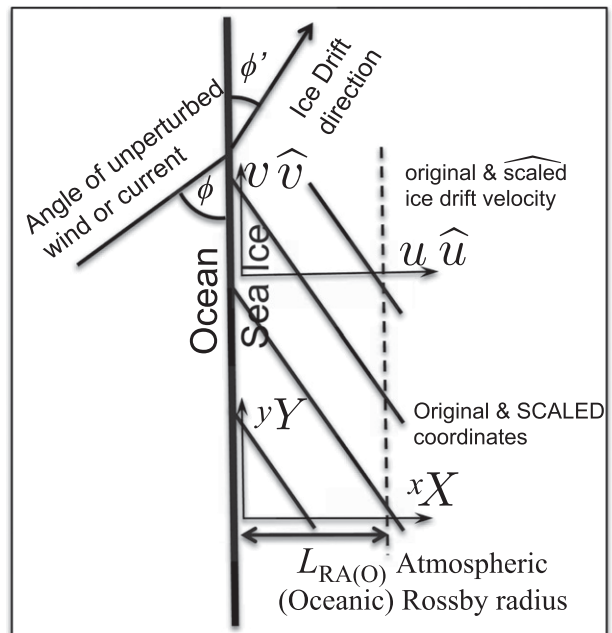


FIG. 5. Coordinate and ice drift velocity notation for the analytical model. This notation is true for the results in section 5.

a simplified model of sea ice drift is derived. The model uses the momentum balance of Gray and Morland (1994) along with the sea ice rheology of Hibler (1979) and is simplified to give one-dimensional solutions. The model equations used are similar to the ice edge model of Lepparanta and Hibler (1985), where a two-dimensional numerical grid was used to seek solutions. Our model finds analytical solutions to the equations using a methodology similar to Feltham (2005), although granular dynamics have not been considered in this study.

Coordinate and velocity notation for this section is given in Fig. 5, with notation from section 2 no longer used. To model the movement of sea ice during the formation of oceanic and atmospheric jets, the momentum balance of Gray and Morland (1994) is used, giving solutions for a dynamically changing ice drift velocity and ice concentration. This momentum balance considers the sea ice ocean mixture layer containing the ice floes and the ocean between them down to the depth of the floes. The interactions between the ice floes and the ocean between them are described as a continuum, over a length scale greater than individual floe dimensions. The momentum balance for the mixture layer is constructed by considering momentum balances for both the ice and ocean and integrating vertically over the layer. The rate of change of momentum of the layer is given by

$$m \left(\frac{\partial \mathbf{u}}{\partial t} + \mathbf{u} \cdot \nabla \mathbf{u} \right) = -mf_c \mathbf{k} \times \mathbf{u} + A\tilde{\tau}^a + A\tilde{\tau}^o + \mathbf{S} + \nabla \cdot \boldsymbol{\sigma}, \quad (12)$$

where m is the mass of sea ice, \mathbf{u} is the velocity of the mixture layer, f_c is the Coriolis parameter, A is the ice concentration ($A = 0$ is for open ocean, and $A = 1$ is for a complete ice cover), $\tilde{\tau}^a$ and $\tilde{\tau}^o$ are the applied atmospheric and oceanic stresses, \mathbf{S} is the ocean surface tilt force (neglected for this study), and $\boldsymbol{\sigma}$ is the ice stress tensor. The applied stresses are calculated from Eqs. (5) and (4), and their role in the balance depends upon the ice concentration, applying the external stresses to only the ice in the layer.

For a continuum sea ice model at a length scale greater than individual sea ice floes, the dynamics of the sea ice can be assumed to be isotropic at the sea ice edge [but see Feltham (2008) for a fuller discussion of the issues]. Here we assume that the rheology of the sea ice may be described using the viscous plastic (VP) rheology of Hibler (1979). For typical stress levels in the VP rheology, the ice deforms as a plastic. In plastic deformation, energy is lost in deforming the ice. This lost energy creates features such as ridges or leads (cracks that can extend for many kilometers). For low stresses the sea ice is taken as a viscous fluid. The transition from viscous to plastic deformation happens at the yield stress. This yield stress is expressed as a curve in principle stress space.

The ice stress tensor σ_{ij} is related to the strain rate of the sea ice, defined by

$$\dot{\epsilon}_{ij} = \frac{1}{2} \left(\frac{\partial u_i}{\partial x_j} + \frac{\partial u_j}{\partial x_i} \right), \quad (13)$$

where $(i, j) = (x, y)$ are directional indices. The stress invariants of negative pressure σ_I and maximum shear rate σ_{II} are related to the principle stresses σ_1, σ_2 by

$$\sigma_I = 0.5(\sigma_1 + \sigma_2) \quad \text{and} \quad \sigma_{II} = 0.5(-\sigma_1 + \sigma_2).$$

The VP stress tensor is calculated from

$$\sigma_{ij} = 2\eta\dot{\epsilon}_{ij} + (\zeta - \eta)\dot{\epsilon}_{kk}\delta_{ij} - 0.5p\delta_{ij}, \quad (14)$$

where η and ζ are the shear and bulk viscosities, and p is the ice pressure. The shear and bulk viscosities are given by

$$\eta = \frac{\zeta}{e^2}, \quad (15a)$$

$$\zeta = \frac{p}{2\Delta}, \quad \text{and} \quad (15b)$$

$$\Delta = [(\dot{\epsilon}_{11}^2 + \dot{\epsilon}_{22}^2)(1 + e^{-2}) + 4e^{-2}\dot{\epsilon}_{12}^2 + 2\dot{\epsilon}_{11}\dot{\epsilon}_{22}(1 - e^{-2})]^{1/2}, \quad (15c)$$

where e defines the yield curve's aspect ratio. Hibler (1979) gives

$$p = p^*hg(A) \quad \text{with} \quad g(A) = e^{-c(1-A)}, \quad (16)$$

where p^* is a constant, and h is the ice thickness. The function $g(A)$ is used to represent the amount of floe contact in the ice pack (Gray and Morland 1994) with $g(A = 0) = 0$ and $g(A = 1) = 1$. This parameterization of the ice strength gives a linear relationship between the strength and thickness for high concentrations. As the concentration decreases the ice strength falls significantly. A numerically efficient version of the VP rheology has been implemented in the CICE model (Hunke and Dukowicz 1997).

a. Model equations

The momentum balance of Eq. (12) is solved in order to model the changing sea ice drift velocity (u, v) and concentration A during on-ice winds and currents that give a stable sea ice edge. The coordinate system is aligned with the ice edge, with x normal and y parallel to the edge. We consider an infinite, laterally invariant ice edge in a steady state so that $\partial/\partial t = 0$ and $\partial/\partial y = 0$. The MIZ is viewed as a region of constant ice thickness with $h = 1$ m. These simplifications are similar to those used by Lepparanta and Hibler (1985) in their study of MIZ dynamics. As the sea ice edge is compacted to form a steady state, the ice drift normal to the sea ice edge u is taken as small and positive for x increasing into the pack. This value is taken to be constant throughout the solution ($\partial u/\partial x = 0$), and the constraint is enough to ensure that the solution for the sea ice concentration increases to near 90% a short distance ($x < \mathcal{L}_R, X < 1$) from the sea ice edge. The components of Eq. (12) under these simplifications become

$$0 = \rho h v + A(\tau_1^a + \tau_1^o) + \sigma_{11x}, \quad \text{and} \\ uv_x = -\rho h u + A(\tau_2^a + \tau_2^o) + \sigma_{12x}, \quad (17)$$

with $m = \rho h$, where ρ is the density of sea ice. The values of σ_{11} and σ_{12} can be calculated from Eq. (14). The only nonzero components of the strain rate tensor in Eq. (13) are $\dot{\epsilon}_{12} = \dot{\epsilon}_{21} = v_x/2$ (15), so that the desired components of the stress tensor are

$$\sigma_{11} = -\frac{p}{2}, \quad \text{and} \quad (18a)$$

$$\sigma_{12} = \frac{p}{2} \frac{e^{-2}v_x}{(2e^{-2}v_x^2)^{1/2}} = \frac{p}{2\sqrt{2}e} \text{sgn}(v_x). \quad (18b)$$

The ice pressure p is given as a function of ice concentration as in Eq. (16).

The model is applied to a region of ice that is under the influence of jet formation, with a length scale of \mathcal{L}_{RA} for the atmospheric jet and \mathcal{L}_{RO} for the oceanic jet. The model is nondimensionalized over these length scales. For experiments with both jets, the atmospheric Rossby radius will be used as it is an order greater than the oceanic. The applied stresses are also scaled. We substitute Eq. (18) into Eq. (17) and nondimensionalize in velocity $\mathbf{u} \rightarrow U_I \hat{\mathbf{u}}$, where U_I is the typical ice speed, position $(x, y) \rightarrow \mathcal{L}_R(X, Y)$, derivatives $\partial/\partial x \rightarrow (1/\mathcal{L}_R)(\partial/\partial X)$, and applied stress $\hat{\boldsymbol{\tau}}^a \rightarrow \mathcal{T}_a \hat{\boldsymbol{\tau}}^a$, $\hat{\boldsymbol{\tau}}^o \rightarrow \mathcal{T}_o \hat{\boldsymbol{\tau}}^o$ (\mathcal{T} terms are typical stress values defined below) to yield

$$0 = f_c \mathcal{L}_R U_I \hat{v} + \frac{\mathcal{L}_R}{\rho h} (\mathcal{T}_a \hat{\tau}_1^a + \mathcal{T}_o \hat{\tau}_1^o) A - \frac{p^*}{2\rho} \frac{\partial g}{\partial A} \frac{\partial A}{\partial X}, \quad \text{and} \quad (19a)$$

$$U_I^2 \hat{u} \frac{\partial \hat{v}}{\partial X} = -f_c \mathcal{L}_R U_I \hat{u} + \frac{\mathcal{L}_R}{\rho h} (\mathcal{T}_a \hat{\tau}_2^a + \mathcal{T}_o \hat{\tau}_2^o) A + \frac{p^*}{2\sqrt{2}e\rho} \text{sgn}(\hat{v}_X) \frac{\partial g}{\partial A} \frac{\partial A}{\partial X}. \quad (19b)$$

These two equations can be combined to give a system of two ordinary differential equations to solve for \hat{v} and A with

$$g_A A_X - \alpha_1(X, \hat{v}) A - \alpha_2 \hat{v} = 0 \quad \text{and} \quad (20a)$$

$$\hat{v}_X - \beta_1 \text{sgn}(\hat{v}_X) \hat{v} - \beta_2 [X, \hat{v}, \text{sgn}(\hat{v}_X)] A + \beta_3 = 0, \quad (20b)$$

where

$$\alpha_1(X, \hat{v}) = 2 \frac{\mathcal{L}_R}{p^* h} \mathbf{T}_1(X, \hat{u}, \hat{v}), \quad \alpha_2 = 2 \frac{\rho f_c \mathcal{L}_R U_I}{p^*},$$

$$\beta_1 = \frac{f_c \mathcal{L}_R}{U_I \hat{u} \sqrt{2} e}, \quad \beta_3 = \frac{f_c \mathcal{L}_R}{U_I} \quad \text{and}$$

$$\beta_2 [X, \hat{v}, \text{sgn}(\hat{v}_X)] = 2 \frac{\mathcal{L}_R}{\rho h U_I^2 \hat{u}} \left[\mathbf{T}_1(X, \hat{u}, \hat{v}) + \frac{\text{sgn}(\hat{v}_X)}{\sqrt{2} e} \mathbf{T}_2(X, \hat{u}, \hat{v}) \right].$$

The functions $\mathbf{T}_1(X, \hat{u}, \hat{v}) = \mathcal{T}_a \hat{\tau}_1^a(X) + \mathcal{T}_o \hat{\tau}_1^o(X, \hat{u}, \hat{v})$ and $\mathbf{T}_2(X, \hat{u}, \hat{v}) = \mathcal{T}_a \hat{\tau}_2^a(X) + \mathcal{T}_o \hat{\tau}_2^o(X, \hat{u}, \hat{v})$ are derived from the applied stresses with the scaling terms $\mathcal{T}_a = U_A^2 \rho_a C_a$ and $\mathcal{T}_o = U_O^2 \rho_o C_o$. The components of the applied stress terms are calculated from Eqs. (4) and (5).

b. Boundary conditions

Boundary conditions are needed to find a solution for the ice pack. These conditions are derived from the momentum balance of free-drifting sea ice with

$$m \left(\frac{\partial \mathbf{u}}{\partial t} + \mathbf{u} \cdot \nabla \mathbf{u} \right) = -m f_c \mathbf{k} \times \mathbf{u} + \hat{\boldsymbol{\tau}}^a + \hat{\boldsymbol{\tau}}^o, \quad (21)$$

along with an imposed low ice concentration of $A = 0.1$. This nonzero value of A is chosen to represent the sea ice edge. A value of $A = 0$, which would represent the open ocean, results in the solution $A = 0$ for the whole domain. The same simplifications used for the ice pack are applied to the free-drift momentum balance. This models the ice movement at the ice edge where the ice concentration is low, allowing the normal velocity u to be unconstrained. In this model, the region is thin and the solution can be taken as constant throughout, removing all spatial derivatives. The peak values of atmosphere and ocean velocity (at $X = X_{\text{peak}}$) are used for the applied stresses. The ice velocities (\hat{u} , \hat{v}) can be calculated from the components of Eq. (21) with all spatial and time derivatives set to zero. These are a set of simultaneous equations with

$$0 = f_c \hat{v} + \frac{1}{\rho h U_I} \mathbf{T}_1(X_{\text{peak}}, \hat{u}, \hat{v}) \quad \text{and}$$

$$0 = -f_c \hat{u} + \frac{1}{\rho h U_I} \mathbf{T}_2(X_{\text{peak}}, \hat{u}, \hat{v}). \quad (22)$$

To calculate the stress terms (\mathbf{T}_1 , \mathbf{T}_2), typical ice and ocean velocities are needed to calculate u_{diff}^2 . The typical ocean velocity $\tilde{\mathbf{u}}_O = (\sin\phi, \cos\phi)$ is taken as the non-dimensional far-field ocean velocity; the typical ice velocity $\tilde{\mathbf{u}}_I = (\hat{u}, \hat{v})$ is equated to the ice velocity to be solved for. For the case of an ocean jet, the u_{diff}^2 relation is considered. For matching to the ice pack model [Eq. (12)], the parallel component of the velocity \hat{v} is consistent though the normal component \hat{u} is too high to match to the low normal velocity used. A discontinuity in the normal velocity is required. A lower value for \hat{u} can be calculated from Eq. (20b) to maintain continuity in the y direction. Prescribed values of $A = 0.1$, \hat{v} , and the forcing functions \mathbf{T}_1 , \mathbf{T}_2 are used as in the free-drift solution. The derivative \hat{v}_X is set to zero, to maintain continuity, and the derivative A_X is set to be high, anticipating a sharp increase in ice concentration. The term \hat{u} is calculated from

$$0 = -f_c \mathcal{L}_R U_I \hat{u} + \frac{\mathcal{L}_R}{\rho h} A \mathbf{T}_2(X_{\text{peak}}, \hat{u}, \hat{v}) A + \frac{p^*}{2\sqrt{2}e\rho} \text{sgn}(\hat{v}_X) g_A A_X, \quad (23)$$

TABLE 2. Dimensions and lengths of the domains used in the CICE model experiments. The width is in the east–west direction and height the north–south direction. ESD is used to find the sea ice edge in each domain. The sea ice edge in each domain lies approximately on the line of 70°N.

Domain	Resolution	Width (km)	Height (km)	ESD (km)	Grid points
Atmosphere	50 km	1000	1500	75	20 × 30
	10 km	400	800	20	40 × 80
	5 km	200	800	20	40 × 160
	2 km	200	800	5	100 × 400
	1 km	200	800	3	200 × 800
Ocean	1 km	200	400	3	200 × 400
	500 m	100	200	2	200 × 400
	250 m	50	150	1	200 × 600

with \mathbf{T}_1 calculated as for the free drift in Eq. (22), that is, u_{diff}^2 is a function of \hat{u} . For the pack solution, \hat{v} is expected to be at its highest at the sea ice pack–ocean interface. This gives $\hat{v}_X < 0$ with $\text{sgn}(\hat{v}_X) = -1$ for all X .

The coefficient of the highest-order derivative (A_X) in Eq. (20a) is a nonlinear function of A and makes the system of equations difficult to solve using simple analytical methods. Approximating $g(A)$ by a piecewise continuous set of lines over a set of domains \mathcal{D}_i causes the derivative $\partial g/\partial A$ in Eq. (20a) to be constant in each domain (100 domains were chosen to keep the $g(A)$ approximation error less than 1% of the original magnitude). The system can now be solved in each domain, matching the boundary conditions of each domain to its neighbors to create a complete solution. This method is fully described in Heorton (2013).

The solution is started at $X = 0$. Boundary conditions are taken for A and \hat{v} , and Eqs. (20) are solved over \mathcal{D}_1 until $A = A_1$. Values for A , \hat{v} , and X at this point are used as boundary conditions to solve over \mathcal{D}_2 . This process is repeated to give a complete solution for the ice edge. Results from this model are presented in section 5.

4. CICE model configuration

In the analytical model described previously, only the component of the ice velocity parallel to the ice edge is able to vary. The normal component is held constant, restricting the direction in which the ice can deform. The sea ice edge is assumed to be laterally invariant and in steady state, removing all variations along the ice edge. To model an unconstrained sea ice edge with a varying sea ice state CICE is used. This model is widely used in global climate models (GCMs) including the Hadley Centre Global Environmental Model (HadGEM; U.K. Met Office Hadley Centre) and U.S. National Center for Atmospheric Research (NCAR) models. It is designed to work on a grid

covering the entire globe. The model calculates the state of the sea ice from atmospheric and oceanic forcing, considering the thermodynamics and momentum of the sea ice (see Hunke and Lipscomb 2010). The dynamics of sea ice drift are modeled similarly to Hibler (1979), using a numerical implementation of the viscous plastic rheology.

To focus the model upon the sea ice edge, idealized land-free domains with a cyclic east–west boundary were created. These domains give a long straight ice edge at 70°N in the open ocean. The response of the CICE model changes for different model resolutions, as discussed in section 4b. The CICE model was initially run for a period of 2–10 days of model time with a still ocean and atmosphere to calculate the initial conditions with a stable sea ice edge and sharply increasing sea ice concentration. Model runs were then performed with an idealized forcing dataset with uniform on-ice winds or ocean currents, both with and without atmospheric and oceanic jets. Model runs were over 6 h in model time, with a steady state reached within 2 h and remaining constant over the rest of the run.

a. Adding jets to the forcing data

To develop the forcing data to include atmospheric and oceanic jets, individual data points have to be perturbed. The atmosphere and ocean velocity fields are stored in two arrays, the x and y components. To add jets to these fields, two values need to be known for each point in the array: the distance from the point to the ice edge and the angle of the ice edge, which represent ϕ and \hat{n} in Eqs. (8b) and (11b). These values can be calculated by analyzing the ice concentration, which is calculated by the model, and taking values from the grid file.

To find the ice edge, two fields are created. These are areas of ice cover $A > 60\%$ and areas of open ocean $A < 15\%$. Grid cells at the sea ice edge are defined as points of ice cover that are within a certain distance of points of open ocean [the edge search distance (ESD) in Table 2].

This distance varies depending upon the grid resolution and how quickly the ice concentration increases. In the domains used for this study, the ice concentration increases from 0% to near 100% within a few grid cells from the sea ice edge and is not expected to change significantly during the 6 h model time scale used. The edge search distances selected represent the dimensional width of these grid cells.

From the ice edge points the ice edge angle can be calculated. A box of width $2\mathcal{L}_{R(A,O)}$ (for an atmospheric or oceanic Rossby radius, respectively) is drawn around each point. Starting at the edge of each box, a search is performed for other edge points. When another point is found, the geodesic angle between this point and the original point is calculated. During this calculation a check is performed to keep the ice upon the right-hand side (to keep all the ice edge angles consistent). This calculation is repeated several times (we found five calculations were sufficient to give a consistent angle across the ice edge in the grids shown in Table 2) and averaged. If no other ice edge points are found within the box, the original edge point is discounted. This process calculates the direction of the ice edge over a Rossby radius. Wobbles and deviations of a length scale shorter than this are ignored. Also ice edge points that are not part of a continuous edge are discounted.

The thin band of ice edge grid cells is now defined along with the ice edge direction. As the jets cover a distance $\approx 3\mathcal{L}_{R(A,O)}$ away from the ice edge, a thicker band of cells is needed. Setting the distance from the ice edge in the thin band of edge cells as $d = 0$, the band of cells can be thickened by considering each cell and adding all unselected neighboring cells. The distance from the ice edge is increased by considering the grid cell size at this point. The ice edge angle is also passed on to the new points. This process is iterated until a band of width $\approx 6\mathcal{L}_{R(A,O)}$ is created. This distance contains all significant perturbations to the wind or ocean current in both directions from the ice edge.

The jets can now be added to the wind and ocean velocity components of the forcing data. The values needed in Eqs. (8b) and (11b) are $U_{(A,O)}$ taken from the original velocity arrays, \hat{n} calculated by scaling d over a Rossby radius, and ϕ the difference between the ice edge angle and bearing angle of the wind or ocean current (see Fig. 4). This bearing angle can be calculated from the components of the forcing data and the geodesic angle of the grid. For the oceanic jets, the u_{diff}^2 term needs to be considered. The coupled method of calculating this term used in section 3b cannot be used. As the relationship between the ocean current and ice drift velocity and jet formation in the

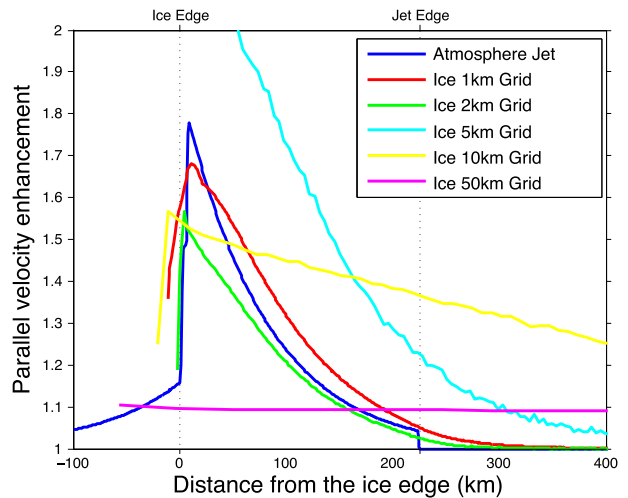


FIG. 6. Parallel velocity enhancement of sea ice drift due to atmospheric jet formation with wind of 5 m s^{-1} at an angle of $\phi = 135^\circ$ to the sea ice edge in the CICE model at different model resolutions. The enhancement of the atmospheric jet (dark blue) and CICE model sea ice drift jet at 1-km resolution (red line) are identical to those presented in Fig. 7b, (dotted-dashed and solid lines, respectively). The model response to jet formation was consistent for resolution of at most 2 km.

CICE model is unknown, a parameterization is used to prescribe the expected ocean jet strength. Experiments using the analytical model were used to create a parameterization of u_{diff}^2 from ϕ with $u_{\text{diff}}^2(\phi) = \mathcal{K} \sin^2 \phi$, where $\mathcal{K} = 1.1$ is a constant. The U_O dependency is not conclusive from the analytical model and so is not considered in calculating u_{diff}^2 for the CICE experiments.

b. Model response at different resolutions

The response of the sea ice to the jets is not the same for all the domains used (Table 2). The same jet experiment was repeated on each domain in order to find at which resolution the response of the sea ice converges to the same solution. For the atmosphere, a wind of 5 m s^{-1} at an angle of $\phi = 135^\circ$ to the ice edge was used. For the ocean a current of 0.2 m s^{-1} at an angle of $\phi = 150^\circ$ to the ice edge was used. The process described in section 4a was used to add the jet to the forcing. The coarsest resolution used was 50 km to represent the resolution commonly used by the sea ice component in global climate models. Higher-resolution domains at 10, 5, 2, and 1 km were also used. The ocean jet was tested at 1-km, 500-m, and 250-m resolution. For detailed plots of the CICE runs at different resolutions, see Heorton (2013, section 6.1.3).

The results for the atmospheric jet approach convergence for the 2- and 1-km resolutions as shown in Fig. 6.

The ice response at these resolutions correlates well with the results from the analytical model. The parallel component of the sea ice velocity from the jet and no jet runs using the 1- and 2-km resolutions, although not identical, has a similar profile that is not matched by the lower-resolution runs. From this, it is concluded that to accurately test the effects of the atmospheric jet upon the sea ice edge, a grid size of at most 2 km must be used. In section 5, the 1-km resolution is used.

There is no clear transition to convergence for the ocean jet. Ice jets form in all domains and have a similar size and shape with similar ice drift speeds in both the jet and no jet runs. As the resolution increases, the ice drift jet approaches the shape of the ocean jet, though it does not have the same correlation as seen with the atmospheric jet on the 1-km grid. When at the high resolutions used for the ocean jet, the ice thickness can alter greatly over the width of the jet, whereas it is near constant over the width of the atmospheric jet. A grid resolution of 500 m has been selected to give a well-defined jet, while keeping a short model run time.

5. Results

Experiments with the analytical and CICE models were performed in pairs, one with uniform forcing and one with a jet perturbed into the forcing depending upon the arrangement of wind, ocean current, and the sea ice edge. For experiments with the atmospheric jet, the ocean was kept still and the atmospheric jet was calculated using Eq. (8). The experiments were repeated to vary the unperturbed surface wind direction ϕ and speed U_A , while keeping low Froude number conditions $\mathcal{F}_A < 1$. For the ocean jet experiments, the atmosphere was kept still. The analytical model was used first as it couples the ocean jet intensity with the sea ice drift solution (the u_{diff}^2 relation in section 4a). The results from the analytical model enabled a parameterization to add the ocean jets to the CICE model. Finally, experiments for specific arrangements of oceanic and atmospheric jets were performed, first with the analytical model to calculate the correct ocean jet strength. The results from the CICE model are averaged across the ice edge for comparison to the laterally invariant analytical model. There is little variation along the ice edge in the CICE model, and the standard deviations to the plotted results are small at $<5\%$ of the mean.

a. Atmospheric jets

Demonstration experiments for a far-field wind speed of $U_A = 5 \text{ m s}^{-1}$ at an angle of $\phi = 135^\circ$ and $\phi = 45^\circ$ to the sea ice edge are shown in Fig. 7. These angles are chosen to show both the positive and negative

contribution of the second-order correction to the jet shape as shown by the dashed lines in Fig. 4. The addition of the jet to the wind over the MIZ increases the wind velocity in a direction parallel to the sea ice edge. The increase is experienced by the sea ice through the applied atmospheric stress. For the demonstration experiments, the momentum of the sea ice [Eq. (12)] is dominated by the atmospheric and oceanic stresses that oppose each other due to the still ocean [for a detailed description see Heorton (2013)]. The ice drift parallel to the sea ice edge increases from near constant through the MIZ (gray lines in Figs. 7a,b) to a faster drift in the direction of the jet formation. The increase is at its greatest at the sea ice edge and decays away to the no jet velocity over 300 km. The increase in velocity component parallel to the sea ice edge is an enhancement $v_{\text{jet}}/v_{\text{no-jet}}$ (where an enhancement of 1 is for no change), which is used to compare the ice drift jet and atmospheric jet strength.

The ice drift jet calculated analytically is shown with a dashed line, the ice drift jet calculated numerically (section 4) is shown with a solid line, and the atmospheric jet enhancement is shown with a dotted-dashed line in Fig. 7. The jets are approximately equal in size and strength (Figs. 7b,d) with the ice drift jet from the analytical model having a greater correlation to the atmospheric jet enhancement. For the analytical model, the atmospheric jet was aligned with the ice edge, with the step change between the positive and negative second-order correction not interacting with the sea ice. In the CICE model, the center of the atmospheric jet cannot be exactly aligned with the ice edge due to the sea ice edge occurring over 10 km of increasing ice concentration. This results in the step change in wind speed occurring over the outer 10–20 km of the sea ice. This results in a step change in ice drift speed and the formation of a “thin atmospheric ice drift jet” over the outer 5–10 km of the MIZ (see solid lines in Figs. 7c,d). For the jet at $\phi = 45^\circ$ to the sea ice edge, there is a significant difference between the CICE and analytical models. This is due to the Coriolis acceleration in the CICE model causing a greater on-ice drift and thus lower parallel drift. The analytical model is unable to give such a relationship as the normal component of ice motion is calculated in the boundary conditions and then held constant. The ice concentration in both models was not imposed and was able to develop in accordance with the model equations. However, the boundary and initial conditions imposed on the models resulted in an increase from 0% to 90% ice concentration over approximately 20 km for all experiments. It then slowly increases to approach 100% over 100–200 km from the sea ice edge. The ice concentration and thickness

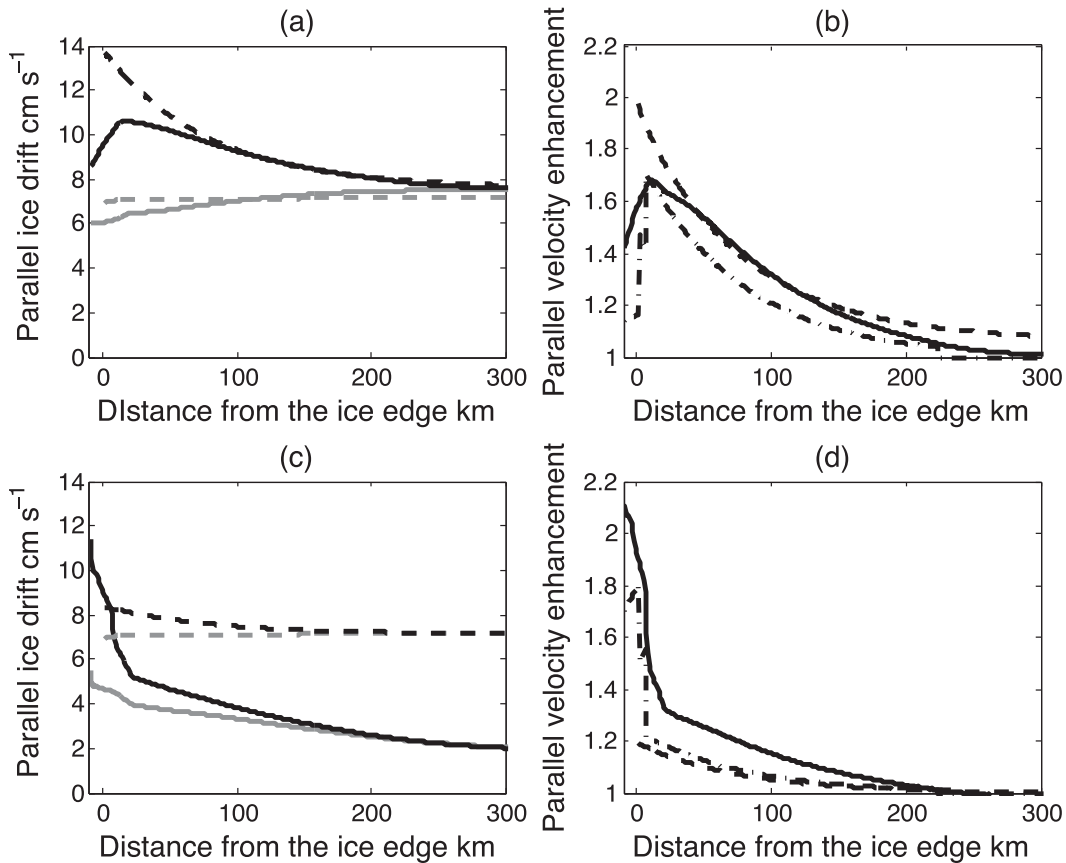


FIG. 7. Ice jet formation due to an atmospheric jet in the Northern Hemisphere with a far-field wind speed of $U_A = 5 \text{ m s}^{-1}$. Solid lines for the CICE model results, dashed for analytical model. (a),(b) For the positive second-order jet over the MIZ ($\phi = 135^\circ$) and (c),(d) the negative ($\phi = 45^\circ$). (a) and (c) show the component of the ice drift velocity parallel to the ice edge during jet (black) and no jet (gray) experiments. (b) and (d) show parallel velocity enhancement where the dotted-dashed lines are the atmospheric jet enhancement.

distribution in the CICE model runs remain similar to the initial conditions described in section 4. We found that changing ice concentration had a limited role in the relationship between the atmospheric, oceanic, and sea ice drift jets and further discussion is not included in this paper. A detailed description can be found in Heorton (2013, sections 5.2.4 and 6.2). The non-dimensional atmospheric and oceanic drag coefficients in the CICE and analytical model were not of the same magnitude, with the analytical model having values approximately twice those of the CICE model to represent the MIZ (1.2×10^{-3} vs 3×10^{-3} for the atmospheric drag and 0.0055 vs 0.011 for the oceanic drag). As both the atmospheric and oceanic drags were increased (due to the increased form drag from floe edges) by a similar magnitude, the ice drift velocity was little altered. A sensitivity study was performed using the analytical model with little variation in ice drift velocity over a range of drag coefficients.

The increased lateral ice drift caused by the formation of the atmospheric jet increases the ice transport parallel to the ice edge. This can be measured by integrating the dimensional ice velocity parallel to the ice edge over the region of the jet, that is, for $0 \text{ km} \leq x \leq 3\mathcal{L}_{RA}$ km. The velocity is multiplied by the ice concentration to give the sea ice fraction of the mixture layer. The transport is given as the horizontal area of sea ice per unit time $\mathcal{A}_{\text{transport}}$ with

$$\mathcal{A}_{\text{transport}} = \frac{\int_0^{3\mathcal{L}_{RA}} Avh \, dx}{\int_0^{3\mathcal{L}_{RA}} h \, dx}, \quad (24)$$

where h is the ice thickness, and v is the component of the ice drift velocity parallel to the sea ice edge as illustrated in Fig. 5. The case of no jet has a parallel drift of $1.4 \times 10^{-2} \text{ km}^2 \text{ s}^{-1}$ for the outer $3\mathcal{L}_{RA}$ of the sea ice

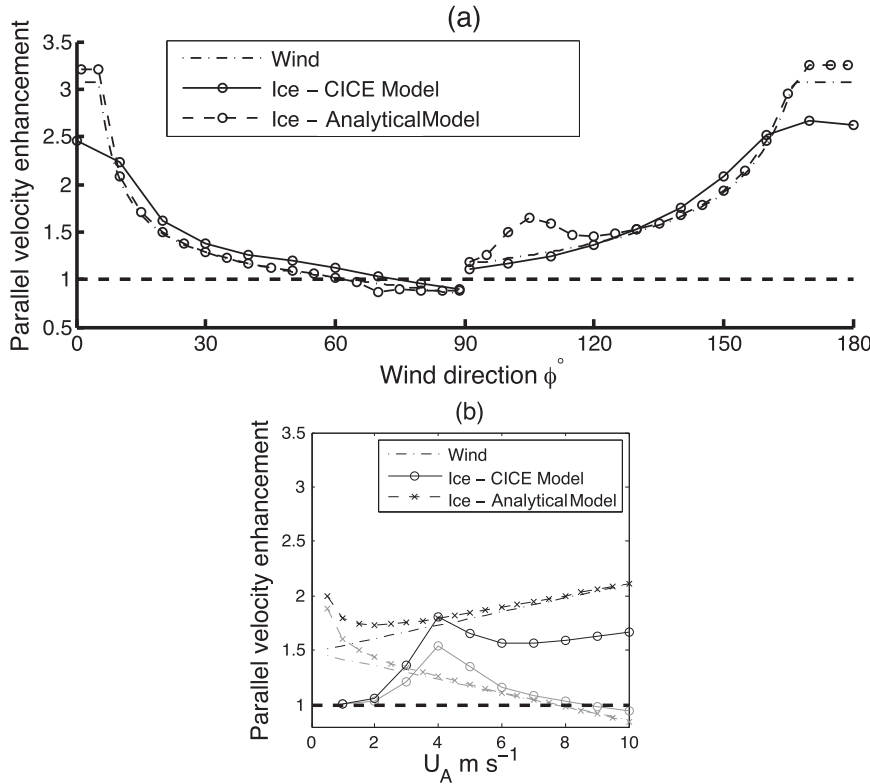


FIG. 8. Atmospheric and ice drift jet strength for varying far-field wind (a) direction and (b) speed. The parallel velocity enhancement is taken at a point 20 km from the sea ice edge. The far-field wind speed in (a) is constant at $U_A = 5 \text{ m s}^{-1}$; the wind directions in (b) at $\phi = 135^\circ$ (black lines) and at $\phi = 45^\circ$ (gray lines). There is a strong correlation between the atmospheric and sea ice drift jets for changing ϕ in (a), though less correlation for changing U_A in (b).

edge for all demonstration calculations except for the $\phi = 45^\circ$ experiment in the CICE model that has a transport of $7.8 \times 10^{-3} \text{ km}^2 \text{ s}^{-1}$. The atmospheric jet formation increases this drift by $5.6 \times 10^{-3} \text{ km}^2 \text{ s}^{-1}$ for the $\phi = 135^\circ$ experiments (a 40% increase) and $1.3 \times 10^{-3} \text{ km}^2 \text{ s}^{-1}$ for the $\phi = 45^\circ$ experiments (a 17% increase).

To view the variations in jet strength due to varying ϕ and U_A , the parallel velocity enhancement at 20 km (so to avoid the thin atmospheric ice drift jet) from the sea ice edge is plotted in Fig. 8. For varying ϕ , the ice drift jet enhancement closely follows the atmospheric jet for both the CICE and analytical models. The only areas of discontinuity are at near-parallel angles where the jet strength plateaus [due to the relation in Eq. (9)] with a lower enhancement for the ice drift jet in the CICE model and near $\phi = 100^\circ$ where there is increased ice drift jet strength in the analytical model. There is less correlation between the atmospheric and ice drift jets in their U_A dependence. The different signs of second-order correction at $\phi = 135^\circ$ and $\phi = 45^\circ$ diverge for increasing wind speed and thus the

Froude number (dotted-dashed lines in Fig. 8). The ice drift jet in the analytical model matches the atmospheric jet for speeds of $U_A > 2 \text{ m s}^{-1}$ and in the CICE model for $U_A > 5 \text{ m s}^{-1}$ in the case of $\phi = 45^\circ$. The case of $\phi = 135^\circ$ has an increasing jet strength but less correlation to the atmospheric jet. Below these speeds, the applied stresses no longer dominate the sea ice momentum balance and are comparable to the Coriolis acceleration and internal ice stresses, which is the cause of the discontinuity at near $\phi = 100^\circ$ in the analytical model. The threshold is lower in the analytical model due to the increased applied stress used to represent the MIZ and the restrictions applied to the ice drift velocity normal to the ice edge.

b. Ocean jets

Demonstration experiments for a far-field ocean current speed of $U_O = 0.2 \text{ m s}^{-1}$ at an angle of $\phi = 150^\circ$ and $\phi = 30^\circ$ to the sea ice edge are shown in Fig. 9. These angles are chosen as they give near-maximal jet enhancement. The addition of the jet to the ocean current causes an increase in velocity parallel to the ice edge

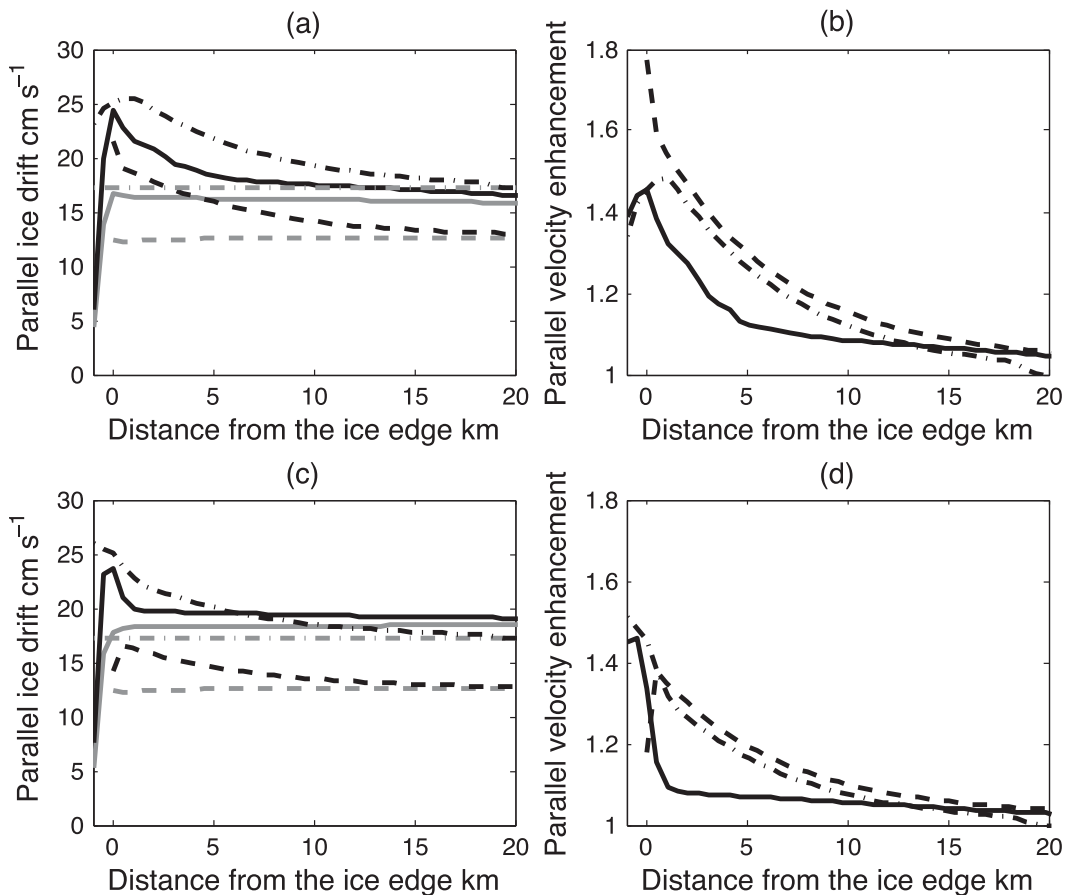


FIG. 9. Ice jet formation due to an oceanic jet in the Northern Hemisphere with a far-field current speed of $U_O = 0.2 \text{ m s}^{-1}$. (a),(b) The positive second-order jet under the MIZ ($\phi = 150^\circ$) and (c),(d) the negative ($\phi = 30^\circ$). (a) and (c) show the component of the ice drift or ocean velocity parallel to the ice edge during jet (black) and no jet (gray) experiments. (b) and (d) show parallel velocity enhancement. Solid lines for the CICE model results, dashed for analytical model, and dotted-dashed for the ocean speeds or enhancement.

extending over 10–20 km (see dotted-dashed lines in Figs. 9a,c) in the direction of the jet formation. The CICE model predicts a parallel ice drift that is near equal to the ocean current for both the jet and no jet cases, whereas the analytical model has a difference of approximately 0.05 m s^{-1} . The ice drift jets in the analytical model (dashed lines) have an enhancement that is closely correlated with the ocean jet (Figs. 9b,d), though the ice drift in the CICE model (dotted-dashed lines) has less correlation primarily due to the variable ice thickness over the outer 10 km.

The ocean jet formation also increases the ice transport parallel to the ice edge. The transport can be calculated as with the atmospheric jet case using Eq. (24) and integrating over the distance $0 \text{ km} \leq x \leq 3\mathcal{L}_{RO} \text{ km}$. As the ocean jet covers a smaller distance into the sea ice pack, the ice transport associated with it is less. For no jet in both cases the ice transport is $0.19 \times 10^{-3} \text{ km}^2 \text{ s}^{-1}$

with an increase of $3.6 \times 10^{-4} \text{ km}^2 \text{ s}^{-1}$ for the $\phi = 150^\circ$ experiments (a 19% increase) and $1.7 \times 10^{-4} \text{ km}^2 \text{ s}^{-1}$ for the $\phi = 30^\circ$ experiments (a 9% increase).

The relationship between the ocean and ice drift jet strength and the angle of incidence ϕ is shown in Fig. 10. Despite the results from the analytical model being used to parameterize the jet strength applied in the CICE model, there is a difference between the ocean enhancements between the two models. This is due to the u_{diff}^2 relation being dependent upon the velocity difference both normal and parallel to the sea ice edge. The normal component is held small and constant in the analytical model due to the assumption that the internal stresses are able to restrict the movement in this direction. The results from the CICE model contradict the assumption of the analytical model. The dimensional ice drift and ocean current speed (for both the jet and no jet runs) are similar for all angles in the CICE model (solid

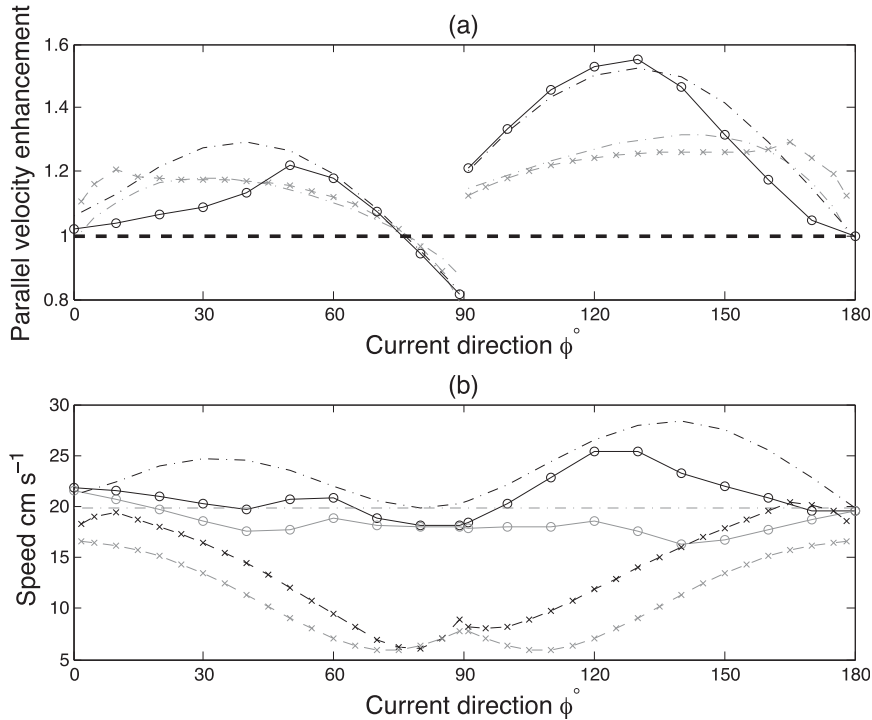


FIG. 10. Oceanic and ice drift jet strength for varying far-field wind direction. (a) Parallel velocity enhancement and (b) the speed taken at a point 2 km from the sea ice edge. Solid lines are for the sea ice in the CICE model, dashed lines for the sea ice in the analytical model, and dotted–dashed lines are for the ocean. Gray lines in (a) are for the analytical model, and the gray lines in (b) are for the no jet experiments. The far-field ocean speed is constant at $U_o = 0.2 \text{ m s}^{-1}$.

and dotted–dashed lines in Fig. 10b), whereas the analytical model has a greater difference for angles near normal to the ice edge. The analytical model gives increased u_{diff}^2 and jet strength for near-normal angles, resulting in the bell curves in Fig. 10a. The CICE model, however, has small u_{diff}^2 over all angles, which should give little or no ocean jet formation for all cases where the ice drift is forced by only ocean currents and internal ice stresses.

c. Combined jets

It is possible that atmospheric and oceanic jet formation can occur simultaneously. This has been considered with the modeling of two arrangements of winds and ocean currents, the first with them aligned in the far field and with $\phi_a = \phi_o = 45^\circ$ (as shown in Fig. 11a) and the second with a separation of 90° with $\phi_a = 135^\circ$ and $\phi_o = 45^\circ$. The sea ice response to the jets was first modeled using the analytical model in order to calculate u_{diff}^2 and the strength and direction of the ocean jet. This information was then used to prescribe the jets into the CICE model.

For the arrangement of aligned wind and ocean current, the ice drift is faster than the ocean current in the

direction parallel to the ice edge. This is required to give the oceanic stress opposing the atmospheric stress. As the ice is moving faster than the ocean, the ocean jet perturbation is negative to the direction of the ocean current, giving a slowing of ocean current at the ice edge (see dotted–dashed lines in Fig. 11a decreasing at 10 km from the sea ice edge). The negative ocean jet results in a negative sea ice drift jet in the analytical model (dashed line), but not in the CICE model (solid line) shown in Fig. 11a. The ice drift over the whole domain in the CICE model is faster and more on ice than the analytical model, and the resulting value of u_{diff}^2 is near zero. This result shows that ocean jet formation due to the ocean current experiencing a sharp change in surface roughness is unlikely when ocean currents are aligned with winds. In this case, as the oceanic stress is slowing down the sea ice drift jet that has formed due to atmospheric forcing, modification to the ocean current could be possible.

For the case of opposing winds and currents with $\phi_a = 135^\circ$ and $\phi_o = 45^\circ$, the sea ice drift in the direction parallel to the sea ice edge is near zero for both the jet and no jet cases (see Fig. 11b), resulting in a value of

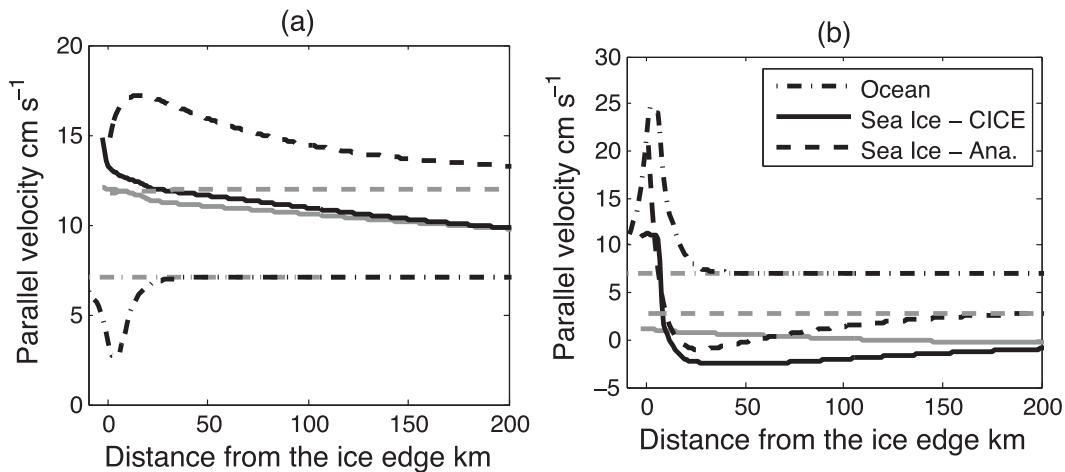


FIG. 11. Sea ice edge response to atmospheric and oceanic jet formation. (a) For aligned wind and ocean current at $\phi_{(a,o)} = 45^\circ$, and (b) for a separation of 90° . The plots show the parallel velocity component for the ocean and sea ice in the CICE and analytical models (see legend); gray lines are for the no jet experiments.

$u_{\text{diff}}^2 \approx 1$ in both the analytical and CICE models and a large ocean jet in the direction of the ocean current. This presents a realistic situation for ocean jet formation at the sea ice edge. The analytical model in this situation gives incorrect internal ice stresses. The ice drift shown in Fig. 11a has a changing $\text{sgn}(v_x)$ (the gradient of the dashed line changes sign at 20 km from the sea ice edge) that is not consistent with assumptions of the model where $\text{sgn}(v_x)$ is set as a constant throughout the domain. This is a feature intrinsic to the simplicity of the analytical model and the reason for the difference between the results from it and the CICE model in Fig. 11b.

6. Discussion

a. Interpretation and validation of results

The response of the sea ice edge to atmospheric and oceanic jet formation has been modeled. The atmospheric jet formation is similar to coastal jets and is driven by the sharp change in surface roughness at the sea ice edge. There is little evidence to either validate or disprove the formation of atmospheric jets as the jet perturbations are over 100 km horizontally compared to the point atmospheric observations that have been made at the sea ice edge [see section 1, in particular Guest et al. (1995) and Andreas et al. (1984)]. The ice drift jets we attribute to the formation of atmospheric jets fit well with those observed by Johannessen et al. (1983). The observed jets have a lateral extent of 250 km, typical ice drift speed of $0.1\text{--}0.2\text{ m s}^{-1}$, and typical wind speed of 10 m s^{-1} with both the wind and ice drift perturbed in the direction parallel to the sea ice edge. The observed

conditions in Fig. 2 can be recreated in the analytical model with a unperturbed surface wind at an angle of $\phi = 5^\circ$ to the sea ice edge and with a speed of 6 m s^{-1} for 19 September and 3 m s^{-1} for 27 September. The close correlation between ice drift modeled in both the analytical and CICE models (see Fig. 8) and the observations discussed here supports the atmosphere–sea ice interaction presented in this paper.

The oceanic jet formation is driven by a sharp change in surface roughness beneath the ice, and the resulting ice drift speed is similar to the ocean current speed. The relative difference between the ocean and sea ice drift velocity u_{diff}^2 has to be considered in order to calculate the jet intensity (see section 2b). The results from the CICE model show that u_{diff}^2 is very small unless there is an opposing wind stress that holds the sea ice still (see Fig. 10). This gives a very low ocean jet strength for most cases and reduces the likelihood of observable ocean jets. The assumption of a well-compacted sea ice edge restricting the movement of the sea ice edge in the analytical model appears to be invalid for strong ocean currents. Further investigation into edge compaction events in the Antarctic (Massom et al. 2006, 2008; King et al. 2010) could give insight into this relationship.

When the sea ice edge is under the influence of both on-ice winds and ocean currents the possible formation of jets has to be carefully considered. Atmospheric jets can be calculated as with a still ocean. As shown in Fig. 11a, when surface winds and ocean currents are aligned, the sea drift is expected to be faster than the ocean current resulting in no ocean jet formation. The Greenland Sea presents such an arrangement of surface wind and ocean currents. The atmospheric Greenland

Sea jet is often aligned with the oceanic East Greenland Current (van Angelen et al. 2011) that interacts with the sea ice edge in the Greenland Sea and Fram Strait. Point observations of the relative velocity of winds, ocean currents, and sea ice drift at the sea ice edge in the Greenland Sea could be used for validation. The arrangement of opposing winds and ocean currents can result in ocean jet formation (see Fig. 11b), though the likelihood of such an arrangement is inconclusive.

b. Areas of likely jet formation

To view possible areas for jet formation, 2 yr of global data from the U.K. Met Office climate model HadGEM3 are analyzed [see Hewitt et al. (2011) for the model description]. Daily ice concentration data are analyzed by the same method used to apply the jets into the CICE model (section 4) to find areas where there is a compact ice edge that is consistent with jet formation. If the surface wind direction over these areas is on ice and subcritical ($U_A < 10.9 \text{ m s}^{-1}$), then an atmospheric jet can form. There are no atmospheric jets apparent in the data that formed due to either the physics represented within the model or a model parameterization.

For the Arctic, the model data give three main areas where atmospheric jets can form: in the Fram Strait, the Greenland Sea, and in the Labrador Sea west of Greenland (see Fig. 12a). There is an ice edge allowing for atmospheric jet formation in these areas for 90%–100% of the data. When considering the winds, these three areas have subcritical on-ice wind allowing for jet formation for 40%–50% of the time or approximately half of the time when there is an ice edge allowing for jet formation (see Fig. 12b). There is another area of possible jet formation that only occurs during the summer. The area of the Arctic Ocean north of the Bering Strait between the Beaufort and East Siberian Seas has a long ice edge that allows for atmospheric jet formation. The interaction between the atmosphere and sea ice edge in this area, in particular the movement of storms, has been studied by Long and Perrie (2012).

For the Antarctic there are two main areas where atmospheric jets can form. One is east of the Antarctic Peninsula in the Weddell Sea. The other is off of East Antarctica between Wilkes Land and the Ross Sea. Both of these areas have an ice edge allowing for jet formation 80%–100% of the time (Fig. 12c). When considering the wind strength and direction, an atmospheric jet would be expected to form around 40%–50% of the time (Fig. 12d).

The Fram Strait Ice Drift (FSID) is given by Kwok (2004) from synthetic aperture radar (SAR) images from 1978 to 2002. The average ice drift in this period is $866\,000 \text{ km}^2 \text{ yr}^{-1}$, which is equivalent to

$\approx 2.8 \times 10^{-2} \text{ km}^2 \text{ s}^{-1}$. When an atmospheric jet forms over the sea edge, the ice drift beneath it is expected to increase. This increase is calculated in section 5 to be $\approx 1.4\text{--}5.6 \times 10^{-3} \text{ km}^2 \text{ s}^{-1}$, with greater values possible for winds parallel to the ice edge. This increase is over the outer 250 km of ice pack compared to the 780-km width of the Fram Strait. The possible ice drift increase due to the formation of an atmospheric jet is significant at 5%–20% of the total ice drift through the Fram Strait. The FSID has been shown to be forced by a wind feature known as the Greenland Sea jet (van Angelen et al. 2011) along with the oceanic East Greenland Current. This jet is driven by temperature and surface gradient differences between the Greenland Ice Sheet and the Greenland Sea. As the atmospheric jets presented in this study are driven by changes in surface roughness [a process not considered by van Angelen et al. (2011)], they could play an additional role in the ice export through the Fram Strait. The FSID is of particular importance during the summer, with the low Arctic sea ice extent of the summers of 2010 and 2011 being partially attributed to the high summer FSID of these years (Ogi and Wallace 2012). The environmental characteristics that allow for atmospheric jet formation (as discussed in section 1) are more likely to be present over the sea ice edge during summer months, and ice drift jets have been observed near the Fram Strait during the summer (Johannessen et al. 1983). During the winter the south Greenland Sea experiences barrier winds (van den Broeke and Gallee 1996) that are southerly winds flowing toward the Greenland Peninsula due to thermal effects. These winds interact with the sea ice edge allowing for jet formation.

The formation of atmospheric jets over the sea ice edge could cause an increase in the formation of deep-ocean water. Pickart et al. (2003) show that the Greenland tip jet, which is of a similar size to the atmospheric jets in this study (of order 100 km wide), makes a significant contribution to open-ocean convection and the formation of ocean deep water. This jet is formed by the cold air mass over the Greenland ice pack flowing out over the Atlantic Ocean. The Greenland tip jet has been modeled by Orr et al. (2005a) and is of similar size and strength to the atmospheric jets calculated in section 2.

7. Conclusions

The theory of Hunt et al. (2004) models the formation of atmospheric jets due to a sharp change in surface roughness. This theory has been applied to the sea ice edge in this paper for the first time, and a new theory of ocean jet formation has been developed (section 2). The ocean jet model required the consideration of jet

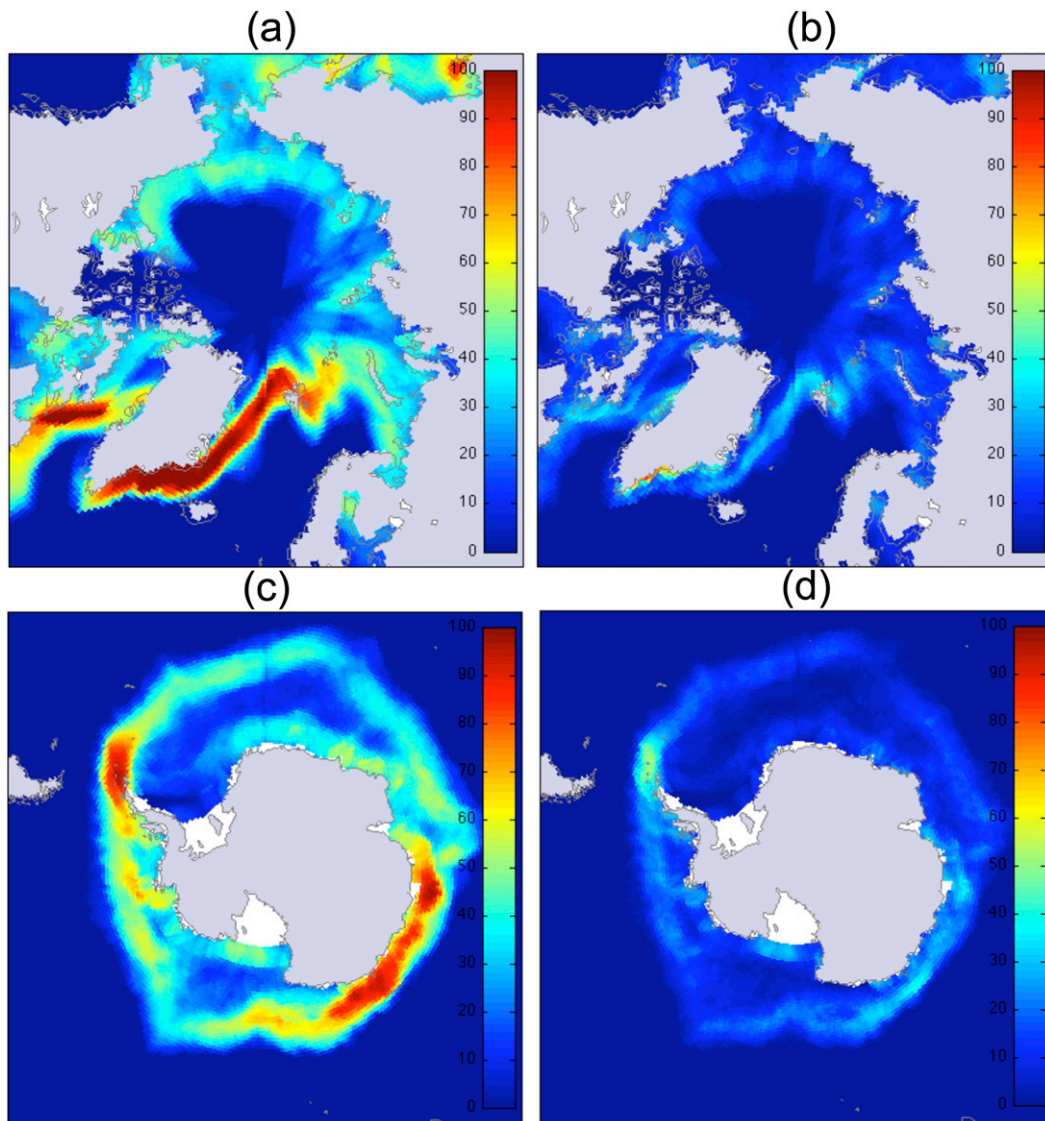


FIG. 12. Areas of possible atmospheric jet formation in the HadGEM3 model (2 yr of daily ice concentration and wind data). (a),(c) Percentage of the data that could contain an atmospheric jet formed over a sea ice edge. (b),(d) The percentage of the data in which the wind direction and strength allow for an atmospheric jet over a sea ice edge. The red areas in (a) and (c) and green in (b) and (d) present conditions for atmospheric jet formation, for example, the Fram Strait and Greenland Sea in (a) and (b).

formation due to a fluid's interaction with a moving band of increased surface roughness. A review of observations and modeling of sea ice roughness in the marginal ice zone has been performed to estimate the increase in surface roughness. This has allowed for the prediction of the size and strength of atmospheric and oceanic jets.

An analytical model of sea ice drift at the sea ice edge was developed (section 3). Most existing studies of sea ice with realistic rheology use numerical models, whereas this model uses several assumptions and novel methods

to achieve analytical solutions. Despite the simplifications and restrictions we have imposed, the analytical model is able to produce realistic solutions for the ice drift during the formation of an atmospheric jet. These results are similar to those produced by the numerical sea ice model CICE (Figs. 7, 8), which uses the same rheology with no restrictions.

The CICE model was used to investigate the sea ice edge. The model was set up at various resolutions to investigate the model's sensitivity to grid resolution (see section 4), and we found that there was only reliable ice

drift jet formation at a resolution of 2 km or higher. This is the first study of its kind. The method of finding an ice edge in a map of ice concentration data has been created for this paper (section 4a). This has allowed for the addition of atmospheric and oceanic jets into forcing data for the CICE model experiments and the analysis of ice concentration data to find possible locations of atmospheric jet formation (Fig. 12).

We have considered the formation of atmospheric jets at the sea ice edge for on-ice surface winds. The shape of the jets features a peak wind speed over the sea ice edge that decays away over several atmospheric Rossby radii (75 km). Oceanic jet formation has also been considered over an oceanic Rossby radius (6 km). The strength of the ocean jet depends upon the difference in speed between the ocean and sea ice edge. To accurately calculate the ocean jet strength, the jet calculation needs to be coupled to the analytical ice drift model as described in section 3b. The results from the analytical model allow the jets to be added to the CICE model as described in section 4a. The results from the CICE model, however, disagree with the analytical model and show that the compaction of the sea ice edge is not sufficient to stop the ice drift normal to the ice edge (Fig. 10). This results in the relative difference between the sea ice and ocean velocities being small, and ocean jet formation is unlikely.

The formation of atmospheric and oceanic jets over the sea ice edge has been shown to result in the formation of a sea ice drift jet. The sea ice drift jet that forms under an atmospheric jet has a similar velocity enhancement to the atmospheric jet (Fig. 8); for example, a wind speed increase of 100% results in an ice drift speed increase of 100%. The sea ice drift jet that results from an atmospheric jet matches an observed sea ice drift jet north of Svalbard (Johannessen et al. 1983), though more detailed observations are needed for validation. The sea ice drift jet is shown to significantly increase the transport of sea ice along the sea ice edge by 40% over the outer 250 km of the sea ice pack. This increase in sea ice transport could be a significant factor in the Fram Strait ice export, an area where atmospheric jet formation is likely to occur over the sea ice edge (Fig. 12). The use of the edge finding and jet applying methods we have developed allow for the consideration of jet formation in a global sea ice model.

Acknowledgments. This project was partly funded by the National Centre for Earth Observation and through a CASE award from the Met Office Hadley Centre. Special thanks go to Ann Keen of the Hadley Centre who was most helpful in the analysis of the HadGEM3 model data and the running of the CICE model.

APPENDIX

Theory of Atmospheric Jet Formation

Hunt et al. (2004) describe and illustrate an atmospheric flow of speed U_A within the ABL of thickness h_A approaching a change in surface roughness length from z_O to z_{It} (O is ocean and It is ice top). The ABL has density ρ_A , and a step change in the air density of magnitude $\rho_A \Delta \widehat{\rho}_A$ exists between the ABL and the less dense inversion layer above it. Here the notation Δ signifies a step change, and $\widehat{\rho}_A$ denotes nondimensional. The equation $\Delta g_A = g \Delta \widehat{\rho}_A$ is the reduced gravitational acceleration at the surface of the ABL.

Mean horizontal wind velocity profiles are given as $[U(z), V(z), W(z) = 0]$, and perturbations to the flow (u', v', w') are calculated. The pressure profile and its perturbation are given as $P(z)$ and p . Upflow conditions at $x \rightarrow -\infty$ are assumed to be steady and uniform in the horizontal plane. The change in surface roughness perturbs the surface shear layer of thickness h_s . The perturbation propagates to the top of the ABL, causing a change in thickness h , giving the inversion layer height as $h_A + h$. The changing turbulent stresses in the shallow layer are represented by the body forces $F(x, y, t)$ and $G(x, y, t)$ in the x and y directions, respectively.

Hunt et al. (2004) model velocity perturbations to the shallow layer using a linearized momentum balance for the perturbations to the flow field. Expressions for pressure ($P + p$), layer thickness perturbation h , and body forces (F, G) are obtained. The change in ABL thickness is linked to the flow perturbation from the continuity equation

$$Dh = -(\bar{u}_x + \bar{v}_y)h_A, \quad (A1)$$

where (\bar{u}, \bar{v}) are the horizontal velocity perturbations (u', v') averaged over the ABL. Horizontal pressure gradients are given as $p_x = \Delta g_A h_x$, $p_y = \Delta g_A h_y$. Combining the pressure perturbations and momentum balance and averaging over the mixed layer ($0 < z < h_A + h$), Hunt et al. (2004) give

$$\begin{aligned} D\bar{u} &= -\Delta g_O h_x + f_c \bar{v} + \bar{F} \quad \text{and} \\ D\bar{v} &= -\Delta g_O h_y - f_c \bar{u} + \bar{G}, \end{aligned} \quad (A2)$$

where D is the total derivative; (\bar{F}, \bar{G}) are the body forces (F, G) averaged over the ABL; the suffix notation for differentiation is used, for example, $(\)_x = \partial/\partial x$; and $D = \partial/\partial t + U_A \partial/\partial x$ is the full derivative. The scaling values for the ABL flow are the atmospheric Froude number $\mathcal{F}_A = U_A/\sqrt{\Delta g_A h_A}$ and the atmospheric Rossby radius $\mathcal{L}_{RA} = \sqrt{\Delta g_A h_A}/f_c$. Equations (A1) and (A2) can be combined to give an equation to be solved for h with

$$D \left(\nabla^2 h - \frac{h}{\mathcal{L}_{RA}^2} - \frac{\mathcal{F}_A^2}{U_A^2} D^2 h \right) = \mathcal{F}_A \frac{h_M}{U_A} \left[\frac{1}{\mathcal{L}_{RA}} (\overline{G}_x - \overline{F}_y) + \frac{\mathcal{F}_A}{U_A} D(\overline{F}_x + \overline{G}_y) \right]. \quad (\text{A3})$$

For the steady state ($\partial/\partial t = 0$), this equation can be integrated in the x direction and scaled to give

$$\hat{\nabla}^2 \hat{h} - \mathcal{F}_O^2 \hat{h}_{XX} - \hat{h} = \hat{R}(X, Y), \quad (\text{A4})$$

where

$$\hat{R}(X, Y) = (\pm) \int_{\mp\infty}^X (\hat{G}_X - \hat{F}_Y)(X') dX' + \mathcal{F}_A (\hat{F}_X + \hat{G}_Y) = \hat{R}^{(0)} + \mathcal{F}_A \hat{R}^{(1)}, \quad (\text{A5})$$

with $(\hat{F}, \hat{G}) = (\mathcal{L}_{RA} \mathcal{F}_A / U_A) (\overline{F}, \overline{G})$. The scaling is done horizontally over the atmospheric Rossby radius $(X, Y) = (x, y) / \mathcal{L}_{RA}$, $\hat{\nabla}^2 = \mathcal{L}_{RA}^2 \nabla^2$ and vertically over the ABL $\hat{h} = h/h_A$. The forcing function $\hat{R}(X, Y)$ is split into a series in the Froude number. This allows the system to be solved for the leading-order $\hat{R}^{(0)}$ and first-order $\hat{R}^{(1)}$ forcing functions. Equations (A1) and (A2) can also be combined to give $(\hat{u}, \hat{v}) = (\overline{u}, \overline{v}) / U_A$ in terms of \hat{h} with

$$\begin{aligned} \hat{u}_{XY} + \frac{\hat{u}_X}{\mathcal{F}_A} &= - \left(\frac{\partial}{\partial Y} + \mathcal{F}_A \right) \frac{\hat{h}_X}{\mathcal{F}_A^2} + \frac{\hat{F}_Y}{\mathcal{F}_A} \quad \text{and} \\ \hat{v}_{XX} - \frac{\hat{v}_Y}{\mathcal{F}_A} &= - \left(\frac{\partial}{\partial Y} - \mathcal{F}_A \right) \frac{\hat{h}_X}{\mathcal{F}_A^2} + \frac{\hat{G}_X}{\mathcal{F}_A}, \end{aligned} \quad (\text{A6})$$

where $(\hat{u}, \hat{v}) = (\overline{u}, \overline{v}) / U_A$ and $(\hat{F}, \hat{G}) = (\mathcal{L}_{RA} \mathcal{F}_A / U_A) (\overline{F}, \overline{G})$.

The body forces (F, G) and the averaged and scaled functions (\hat{F}, \hat{G}) are dependent upon the stress applied to the flow through surface drag. The magnitude of the body forces is the vertical gradients of the perturbation shear stress terms $\partial(-\overline{u'w'})/\partial z$ and $\partial(-\overline{u'v'})/\partial z$. For the atmospheric jets the body forces are parameterized using the perturbation functions ΔC_F and ΔC_G with

$$\begin{aligned} \overline{F} &= - \frac{\Delta C_F U_A^2}{h_A} \quad \text{and} \\ \overline{G} &= - \frac{\Delta C_G U_A^2}{h_A}. \end{aligned} \quad (\text{A7})$$

In the along-wind direction the perturbation ΔC_F is given as

$$\Delta C_F = \Delta_0(z_0) + \Delta_u(\overline{u}), \quad (\text{A8})$$

where $\Delta_0 \approx \kappa^2 [1/\ln^2(h_S/z_{It}) - 1/\ln^2(h_S/z_O)]$ is dependent upon the change in roughness length. For large changes in surface roughness, where $z_{It} \gg z_O$, $\Delta_0 \approx \kappa^2/\ln^2(h_S/z_{It})$, where $\kappa (\approx 0.4)$ is von Kármán's constant. The equation $\Delta_u = C_F(2\overline{u}/U_A - h/h_A)$ is dependent upon the velocity perturbation, with $C_F = \kappa^2/\ln^2(h_S/z_O)$. Through scaling, Hunt et al. (2004) show how the velocity-dependent component Δ_u and the parameter $\Delta C_G \approx C_F \overline{v}/U_A$ can be neglected.

To model the interaction between the atmospheric flow and the sea ice edge, the forcing functions ($\Delta C_F, \Delta C_G$) are given as step functions using the Heaviside step function $\mathcal{H}(\hat{n})$ and its derivative the Dirac delta function $\delta(\hat{n})$. These step functions depend on the angle (ϕ) between the ice edge and the ocean current, see Fig. 4, giving

$$\Delta C_F = |\Delta C_F| \mathcal{H}(\hat{n}), \quad (\text{A9})$$

where $\hat{n} = (x \sin \phi - y \cos \phi) / \mathcal{L}_{RA}$ is the nondimensional distance normal to the ice edge, and $|\Delta C_F|$ is the magnitude of ΔC_F . To solve Eq. (A4), Eqs. (A7) and (A9) are combined. As the forcing components $\hat{R}^{(0,1)}$ both experience a step change at the same location, the calculations can be simplified through their relation to the same function $\Phi(X, Y)$, where

$$\begin{aligned} \Delta C_F &= |\Delta C_F| \Phi_X(X, Y), \\ \hat{F} &= - \widehat{\Delta C}_F \Phi_X(X, Y), \\ \hat{R}^{(0)} &= \widehat{\Delta C}_F \Phi_Y(X, Y) \quad \text{and} \\ \hat{R}^{(1)} &= - \widehat{\Delta C}_F \Phi_{XX}(X, Y), \end{aligned} \quad (\text{A10})$$

with $\widehat{\Delta C}_F = |\Delta C_F| \mathcal{L}_{RA} \mathcal{F}_A / h_A$. Setting $\Phi_X(X, Y) = \mathcal{H}(\hat{n})$, the forcing functions become

$$\hat{R}^{(0)} = - \widehat{\Delta C}_F \frac{\mathcal{H}(\hat{n})}{\tan \phi} \quad \text{and} \quad \hat{R}^{(1)} = - \widehat{\Delta C}_F \frac{\delta(\hat{n})}{\sin \phi}. \quad (\text{A11})$$

Substituting Eqs. (A11) and (A5) into Eq. (A4) gives an equation for \hat{h} that can be solved in the form $\hat{h} = \hat{h}^{(0)} + \mathcal{F}_A \hat{h}^{(1)}$, where

$$\begin{aligned} \hat{h}^{(0)} &= \widehat{\Delta C}_F \frac{J^{(0)}(\hat{n})}{\tan \phi} \quad \text{and} \\ \hat{h}^{(1)} &= \widehat{\Delta C}_F \frac{J^{(1)}(\hat{n})}{\sin \phi}, \quad \text{with} \end{aligned} \quad (\text{A12a})$$

$$J^{(0)}(\hat{n}) = 0.5 [e^{\hat{n}} \mathcal{H}(-\hat{n}) + (2 - e^{-\hat{n}}) \mathcal{H}(\hat{n})] \quad \text{and}$$

$$J^{(1)}(\hat{n}) = 0.5 e^{-|\hat{n}|}. \quad (\text{A12b})$$

From the solutions for the ABL thickness, Eqs. (A6) give a solution for the velocity perturbations. Because

of the low Froude number conditions $\mathcal{F}_A < 1$ assumed in the formulation of the model, Hunt et al. (2004) reduces the Eqs. (A6) to leading order in \mathcal{F}_A , giving

$$\hat{u} = -\frac{\hat{h}_Y}{\mathcal{F}_A} \quad \text{and} \quad \hat{v} = \frac{\hat{h}_X}{\mathcal{F}_A}, \quad (\text{A13})$$

which gives \hat{u} and \hat{v} (in the form $\hat{u} = \hat{u}^{(0)} + \mathcal{F}_A \hat{u}^{(1)}$, see Fig. 4) as

$$\hat{u} = \frac{\widehat{\Delta C}_F}{\mathcal{F}_A} \cos\phi \left[J^{(0)'}(\hat{n}) + \mathcal{F}_A \frac{J^{(1)' }(\hat{n})}{\cos\phi} \right] \quad \text{and}$$

$$\hat{v} = \frac{\widehat{\Delta C}_F}{\mathcal{F}_A} \frac{\cos^2\phi}{\sin\phi} \left[J^{(0)'}(\hat{n}) + \mathcal{F}_A \frac{J^{(1)' }(\hat{n})}{\cos\phi} \right], \quad (\text{A14})$$

where $J^{(0)'}(\hat{n}) = \partial/\partial\hat{n}[J^{(0)}] = 0.5e^{-|\hat{n}|}$ and $J^{(1)' }(\hat{n}) = \partial/\partial\hat{n}[J^{(1)}] = -0.5e^{-|\hat{n}|}\text{sgn}(\hat{n})$ are derivatives of Eqs. (A12b).

REFERENCES

Anderson, R. J., 1987: Wind stress measurements over rough ice during the 1984 marginal ice zone experiment. *J. Geophys. Res.*, **92**, 6933–6941, doi:10.1029/JC092iC07p06933.

Andreas, E. L., W. B. Tucker III, and S. F. Ackley, 1984: Atmospheric boundary-layer modification, drag coefficient, and surface heat flux in the Antarctic marginal ice zone. *J. Geophys. Res.*, **89**, 649–661, doi:10.1029/JC089iC01p00649.

—, K. J. Claffy, and A. P. Makshtas, 2000: Low-level atmospheric jets and inversions over the western Weddell Sea. *Bound.-Layer Meteor.*, **97**, 459–486, doi:10.1023/A:1002793831076.

Belcher, S., T. Newley, and J. Hunt, 1993: The drag on an undulating surface induced by the flow of a turbulent boundary-layer. *J. Fluid Mech.*, **249**, 557–596, doi:10.1017/S0022112093001296.

Bennett, T. J., Jr., and K. Hunkins, 1986: Atmospheric boundary layer modification in the marginal ice zone. *J. Geophys. Res.*, **91**, 13 033–13 044, doi:10.1029/JC091iC11p13033.

Birnbaum, G., and C. Lupkes, 2002: A new parameterization of surface drag in the marginal sea ice zone. *Tellus*, **54A**, 107–123, doi:10.1034/j.1600-0870.2002.00243.x.

Brümmer, B., B. Busack, H. Hoerber, and G. Kruspe, 1994: Boundary-layer observations over water and Arctic sea-ice during on-ice air flow. *Bound.-Layer Meteor.*, **68**, 75–108, doi:10.1007/BF00712665.

Chechin, D. G., C. Lüpkes, I. A. Repina, and V. M. Gryanik, 2013: Idealized dry quasi 2-D mesoscale simulations of cold-air outbreaks over the marginal sea ice zone with fine and coarse resolution. *J. Geophys. Res.*, **118**, 8787–8813, doi:10.1002/jgrd.50679.

Csanady, G. T., 2001: *Air–Sea Interaction: Laws and Mechanisms*. Cambridge University Press, 239 pp.

Drennan, W. M., H. C. Graber, D. Hauser, and C. Quentin, 2003: On the wave age dependence of wind stress over pure wind seas. *J. Geophys. Res.*, **108**, 8062, doi:10.1029/2000JC000715.

Fairall, C. W., and R. Markson, 1987: Mesoscale variations in surface stress, heat fluxes, and drag coefficient in the marginal ice zone during the 1983 marginal ice zone experiment. *J. Geophys. Res.*, **92**, 6921–6932, doi:10.1029/JC092iC07p06921.

—, E. F. Bradley, J. E. Hare, A. A. Grachev, and J. B. Edson, 2003: Bulk parameterization of air–sea fluxes: Updates and verification for the COARE algorithm. *J. Climate*, **16**, 571–591, doi:10.1175/1520-0442(2003)016<0571:BPOASF>2.0.CO;2.

Feltham, D. L., 2005: Granular flow in the marginal ice zone. *Philos. Trans. Roy. Soc.*, **A363**, 1677–1700, doi:10.1098/rsta.2005.1601.

—, 2008: Sea ice rheology. *Annu. Rev. Fluid Mech.*, **40**, 91–112, doi:10.1146/annurev.fluid.40.111406.102151.

Fer, I., and A. Sundfjord, 2007: Observations of upper ocean boundary layer dynamics in the marginal ice zone. *J. Geophys. Res.*, **112**, C04012, doi:10.1029/2005JC003428.

Garratt, J. R., 1992: *The Atmospheric Boundary Layer*. Cambridge University Press, 316 pp.

Gray, J., and L. W. Morland, 1994: A two-dimensional model for the dynamics of sea ice. *Philos. Trans. Roy. Soc. London*, **A347**, 219–290, doi:10.1098/rsta.1994.0045.

Guest, P. S., and K. Davidson, 1991: The aerodynamic roughness of different types of sea ice. *J. Geophys. Res.*, **96**, 4709–4721, doi:10.1029/90JC02261.

—, J. W. Glendening, and K. L. Davidson, 1995: An observational and numerical study of wind stress variations within marginal ice zones. *J. Geophys. Res.*, **100**, 10 887–10 904, doi:10.1029/94JC03391.

Heorton, H., 2013: Jet formation at the sea ice edge. Ph.D. thesis, University College London, 160 pp. [Available online at <http://discovery.ucl.ac.uk/1391815/>.]

Herman, A., 2010: Sea-ice floe-size distribution in the context of spontaneous scaling emergence in stochastic systems. *Phys. Rev. E: Stat. Nonlinear Soft Matter Phys.*, **81**, 066123, doi:10.1103/PhysRevE.81.066123.

Hewitt, H. T., D. Copsey, I. D. Culverwell, C. M. Harris, R. S. R. Hill, A. B. Keen, A. J. McLaren, and E. C. Hunke, 2011: Design and implementation of the infrastructure of HadGEM3: The next-generation Met Office climate modelling system. *Geosci. Model Dev.*, **4**, 223–253, doi:10.5194/gmd-4-223-2011.

Hibler, W. D. I., 1979: A dynamic thermodynamic sea ice model. *J. Phys. Oceanogr.*, **9**, 815–846, doi:10.1175/1520-0485(1979)009<0815:ADTSIM>2.0.CO;2.

Houghton, D. M., 1992: *Wind Strategy*. Fenhurst Books, 91 pp.

Hunke, E. C., and J. K. Dukowicz, 1997: An elastic–viscous–plastic model for sea ice dynamics. *J. Phys. Oceanogr.*, **27**, 1849–1867, doi:10.1175/1520-0485(1997)027<1849:AEVPMF>2.0.CO;2.

—, and W. H. Lipscomb, 2010: CICE: The Los Alamos Sea Ice Model documentation and software user’s manual version 4.1. T-3 Fluid Dynamics Group, Los Alamos National Laboratory Tech. Rep. LA-CC-06-012, 76 pp.

Hunt, J. C. R., A. Orr, J. W. Rottman, and R. Capon, 2004: Coriolis effects in mesoscale flows with sharp changes in surface conditions. *Quart. J. Roy. Meteor. Soc.*, **130**, 2703–2731, doi:10.1256/qj.04.14.

Jarmalavicius, D., J. Satkunas, G. Zilinskas, and D. Pupiennis, 2012: The influence of coastal morphology on wind dynamics. *Est. J. Earth Sci.*, **61**, 120–130, doi:10.3176/earth.2012.2.04.

Johannessen, O. M., J. A. Johannessen, J. Morison, B. A. Farrelly, and E. A. Svendsen, 1983: Oceanographic conditions in the marginal ice zone north of Svalbard in early fall 1979 with an emphasis on mesoscale processes. *J. Geophys. Res.*, **88**, 2755–2769, doi:10.1029/JC088iC05p02755.

- Kantha, L., and G. Mellor, 1989: A numerical model of the atmospheric boundary layer over a marginal ice zone. *J. Geophys. Res.*, **94**, 4959–4970, doi:10.1029/JC094iC04p04959.
- King, J. C., M. J. Doble, and P. R. Holland, 2010: Analysis of a rapid sea ice retreat event in the Bellingshausen Sea. *J. Geophys. Res.*, **115**, C12030, doi:10.1029/2010JC006101.
- Kwok, R., G. F. Cunningham, and S. S. Pang, 2004: Fram Strait sea ice outflow. *J. Geophys. Res.*, **109**, C01009, doi:10.1029/2003JC001785.
- Lepparanta, M., and W. Hibler, 1985: The role of plastic ice interaction in marginal ice zone dynamics. *J. Geophys. Res.*, **90**, 11 899–11 909, doi:10.1029/JC090iC06p11899.
- Long, Z., and W. Perrie, 2012: Air-sea interactions during an Arctic storm. *J. Geophys. Res.*, **117**, D15103, doi:10.1029/2011JD016985.
- Lu, P., Z. J. Li, Z. H. Zhang, and X. L. Dong, 2008: Aerial observations of floe size distribution in the marginal ice zone of summer Prydz Bay. *J. Geophys. Res.*, **113**, C02011, doi:10.1029/2006JC003965.
- Lüpkes, C., and G. Birnbaum, 2005: Surface drag in the Arctic marginal sea-ice zone: A comparison of different parameterisation concepts. *Bound.-Layer Meteor.*, **117**, 179–211, doi:10.1007/s10546-005-1445-8.
- , V. M. Gryanik, J. Hartmann, and E. L. Andreas, 2012: A parametrization, based on sea ice morphology, of the neutral atmospheric drag coefficients for weather prediction and climate models. *J. Geophys. Res.*, **117**, D13112, doi:10.1029/2012JD017630.
- Markus, T., 1999: Results from an ECMWF-SSM/I forced mixed layer model of the Southern Ocean. *J. Geophys. Res.*, **104**, 15 603–15 620, doi:10.1029/1999JC900080.
- Maslowski, W., J. Clement Kinney, M. Higgins, and A. Roberts, 2012: The future of Arctic sea ice. *Annu. Rev. Earth Planet. Sci.*, **40**, 625–654, doi:10.1146/annurev-earth-042711-105345.
- Massom, R. A., and Coauthors, 2006: Extreme anomalous atmospheric circulation in the west Antarctic Peninsula region in austral spring and summer 2001/02, and its profound impact on sea ice and biota. *J. Climate*, **19**, 3544–3571, doi:10.1175/JCLI3805.1.
- , S. E. Stammerjohn, W. Lefebvre, S. A. Harangozo, N. Adams, T. A. Scambos, M. J. Pook, and C. Fowler, 2008: West Antarctic Peninsula sea ice in 2005: Extreme ice compaction and ice edge retreat due to strong anomaly with respect to climate. *J. Geophys. Res.*, **113**, C02S20, doi:10.1029/2007JC004239.
- McPhee, M. G., G. A. Maykut, and J. H. Morison, 1987: Dynamics and thermodynamics of the ice/upper ocean system in the marginal ice zone of the Greenland Sea. *J. Geophys. Res.*, **92**, 7017–7031, doi:10.1029/JC092iC07p07017.
- , R. Kwok, R. Robins, and M. Coon, 2005: Upwelling of Arctic pycnocline associated with shear motion of sea ice. *Geophys. Res. Lett.*, **32**, L10616, doi:10.1029/2004GL021819.
- Ogi, M., and J. M. Wallace, 2012: The role of summer surface wind anomalies in the summer Arctic sea ice extent in 2010 and 2011. *Geophys. Res. Lett.*, **39**, L09704, doi:10.1029/2012GL051330.
- Orr, A., E. Hanna, J. C. R. Hunt, J. Cappelen, K. Steffen, and A. G. Stephens, 2005a: Characteristics of stable flows over southern Greenland. *Pure Appl. Geophys.*, **162**, 1747–1778, doi:10.1007/s00024-005-2691-x.
- , J. Hunt, R. Capon, J. Sommeria, D. Cresswell, and A. Owinoh, 2005b: Coriolis effects on wind jets and cloudiness along coasts. *Weather*, **60**, 291–299, doi:10.1256/wea.219.04.
- Padman, L., and T. M. Dillon, 1991: Turbulent mixing near the Yermak Plateau during the coordinated eastern Arctic experiment. *J. Geophys. Res.*, **96**, 4769–4782, doi:10.1029/90JC02260.
- Pedersen, L. T., and M. Coon, 2004: A sea ice model for the marginal ice zone with an application to the Greenland Sea. *J. Geophys. Res.*, **109**, C03008, doi:10.1029/2003JC001827.
- Pickart, R. S., M. A. Spall, M. H. Ribergaard, G. W. K. Moore, and R. F. Milliff, 2003: Deep convection in the Irminger Sea forced by the Greenland tip jet. *Nature*, **424**, 152–156, doi:10.1038/nature01729.
- Quadfasel, D., J. C. Gascard, and K. P. Koltermann, 1987: Large-scale oceanography in Fram Strait during the 1984 marginal ice zone experiment. *J. Geophys. Res.*, **92**, 6719–6728, doi:10.1029/JC092iC07p06719.
- Roed, L. P., and J. J. O'Brien, 1983: A coupled ice-ocean model of upwelling in the marginal ice zone. *J. Geophys. Res.*, **88**, 2863–2872, doi:10.1029/JC088iC05p02863.
- Shaw, W. J., T. P. Stanton, M. G. McPhee, and T. Kikuchi, 2008: Estimates of surface roughness length in heterogeneous under-ice boundary layers. *J. Geophys. Res.*, **113**, C08030, doi:10.1029/2007JC004550.
- Simpson, J. E., 2007: *Sea Breeze and Local Winds*. Cambridge University Press, 252 pp.
- Thorpe, S. A., 2005: *The Turbulent Ocean*. Cambridge University Press, 439 pp.
- Tisler, P., T. Vihma, G. Müller, and B. Brümmer, 2008: Modelling of warm-air advection over Arctic sea ice. *Tellus*, **60A**, 775–788, doi:10.1111/j.1600-0870.2008.00316.x.
- Tjernström, M., 2005: The summer Arctic boundary layer during the Arctic Ocean Experiment 2001 (AOE-2001). *Bound.-Layer Meteor.*, **117**, 5–36, doi:10.1007/s10546-004-5641-8.
- Toole, J. M., M. L. Timmermans, D. K. Perovich, R. A. Krishfield, A. Proshutinsky, and J. A. Richter-Menge, 2010: Influences of the ocean surface mixed layer and thermohaline stratification on Arctic sea ice in the central Canada basin. *J. Geophys. Res.*, **115**, C10018, doi:10.1029/2009JC005660.
- van Angelen, J. H., M. R. van den Broeke, and R. Kwok, 2011: The Greenland Sea jet: A mechanism for wind-driven sea ice export through Fram Strait. *Geophys. Res. Lett.*, **38**, L12805, doi:10.1029/2011GL047837.
- van den Broeke, M. R., and H. Gallee, 1996: Observation and simulation of barrier winds at the western margin of the Greenland Ice Sheet. *Quart. J. Roy. Meteor. Soc.*, **122**, 1365–1383, doi:10.1002/qj.49712253407.
- Vihma, T., and B. Brummer, 2002: Observations and modelling of the on-ice and off-ice air flow over the northern Baltic Sea. *Bound.-Layer Meteor.*, **103**, 1–27, doi:10.1023/A:1014566530774.
- , J. Hartmann, and C. Lüpkes, 2003: A case study of an on-ice air flow over the Arctic marginal sea-ice zone. *Bound.-Layer Meteor.*, **107**, 189–217, doi:10.1023/A:1021599601948.
- Williams, G. D., S. Nicol, B. Raymond, and K. Meiners, 2008: Summertime mixed layer development in the marginal sea ice zone off the Mawson coast, East Antarctica. *Deep-Sea Res. II*, **55**, 365–376, doi:10.1016/j.dsr2.2007.11.007.